

# APPLIED PHYSICS REVIEWS—FOCUSED REVIEW

## Mechanical behaviors of nanowires

Yujie Chen,<sup>1,2,a)</sup> Xianghai An,<sup>1,a)</sup> and Xiaozhou Liao<sup>1,a)</sup>

<sup>1</sup>*School of Aerospace, Mechanical and Mechatronic Engineering, The University of Sydney, Sydney, New South Wales 2006, Australia*

<sup>2</sup>*School of Mechanical Engineering, University of Adelaide, Adelaide, South Australia 5005, Australia*

(Received 10 June 2017; accepted 18 August 2017; published online 14 September 2017)

The mechanical behaviors of nanowires (NWs) are significantly different from those of their bulk materials because of their small dimensions. Determining the mechanical performance of NWs and understanding their deformation behavior are crucial for designing and manufacturing NW-based devices with predictable and reproducible operation. Owing to the difficulties to manipulate these nanoscale materials, nanomechanical testing of NWs is always challenging, and errors can be readily introduced in the measured mechanical data. Here, we survey the techniques that have been developed to quantify the mechanical properties and to understand the deformation mechanisms of NWs. We also provide a general review of the mechanical properties and deformation behaviors of NWs and discuss possible sources responsible for the discrepancy of measured mechanical properties. The effects of planar defects on the mechanical behavior of NWs are also reviewed.

Published by AIP Publishing. [<http://dx.doi.org/10.1063/1.4989649>]

## TABLE OF CONTENTS

I. INTRODUCTION .....	1
II. EXPERIMENTAL TECHNIQUES FOR NANOMECHANICAL TESTING.....	2
A. Bending.....	2
B. Resonance.....	5
C. Uniaxial loading .....	6
D. Nanoindentation.....	8
III. MECHANICAL BEHAVIORS OF NWs .....	8
A. Young's modulus .....	8
B. Elastic strain.....	10
C. Poisson's ratio .....	12
D. Anelasticity .....	13
E. Strength.....	13
F. Plasticity .....	15
G. Fatigue .....	18
IV. EFFECTS OF PLANAR DEFECTS ON THE MECHANICAL BEHAVIOURS OF NWs .....	19
V. SUMMARY AND CONCLUDING REMARKS .....	24

### I. INTRODUCTION

Nanowires (NWs), which are one-dimensional nanostructures with diameters of the order of 100 nm, have been envisioned as the fundamental building blocks of nanotechnology.<sup>1–4</sup> In the past two decades, the research of NWs has undergone significant expansion, becoming one of the most active research areas in nanoscience and nanotechnology.

<sup>a)</sup>Authors to whom correspondence should be addressed: yujie.chen@adelaide.edu.au, Xianghai.an@sydney.edu.au, and xiaozhou.liao@sydney.edu.au

The significant progress in the fabrication and synthesis of NWs<sup>5–7</sup> has enabled the exploration of their unique and novel mechanical, electrical, magnetic, optical, and catalytic properties, which endows them promising potentials as critical components to architecture nano-electro-mechanical systems (NEMS) with unprecedented functionality.<sup>8–17</sup> With respect to the development of NWs-based nanodevices, apart from physical and chemical properties, the mechanical properties of NWs are another crucial concern, since these devices would be subjected to external forces and large deformation during service. The mechanical properties of NWs including Young's modulus, elastic strain, and plastic strain are important for both the reliability and optimum design of NW-based devices. In addition, when strain is imposed on the semiconductors, their band structures will be changed, which subsequently alters many materials' properties including band gap, effective mass, carrier mobility, diffusivity of dopants, and oxidation rate.<sup>18–25</sup> This is the well-known strain engineering. For example, mechanical bending a CdSe NW has been successfully used to tune the wavelength of laser produced from the NW.<sup>26</sup> However, compared with their functional properties, the mechanical behaviors of NWs have been less informed. Timely exploring the knowledge of the mechanical performance of NWs is important both scientifically, for the in-depth comprehension of deformation behavior of nanoscale materials, and technologically, for the development, design, and manufacture of NWs-based devices and materials with predictable and reproducible operation.<sup>27,28</sup>

It is well known that material dimensions have significant effects on the mechanical behavior of materials, particularly when the dimensions are reduced to the nanometer regime.<sup>29–34</sup> Characterizing the mechanical properties and

understanding the deformation behavior of NWs have been challenging due to the difficulty of mechanical testing of nanoscale objects.<sup>35</sup> Recent development of experimental, computational, and theoretical approaches has catalyzed the exploration of microstructures, deformation mechanisms, and mechanical properties of individual NWs.

Compared with their bulk counterparts, many NWs exhibit unusual mechanical properties because a large fraction of miscoordinated atoms residing at surfaces plays an increasingly significant role in elastic and plastic deformation by reducing the NW dimensions.<sup>40–58</sup>

At early stages, two major approaches of theoretical calculations/simulations, molecular-dynamics (MD) simulations and first-principles calculations,<sup>59–63</sup> were mainly applied to explore the mechanical properties and deformation mechanisms of NWs, in lieu of direct nanomechanical measurements. They are powerful and helpful for the investigations of the deformation behavior of NWs because they enable real-time observation of NW deformation processes at the atomic scale and, at the same time, provide stress-strain curves.<sup>59–62</sup> However, theoretical approaches have unavoidable limitations. The results obtained from computational methods are strongly dependent on the parameters and theoretical functions used.<sup>39,64</sup> Because of the limit of computational capabilities, theoretical calculations have only been used to study NWs with relatively small diameters, usually below 15 nm.<sup>60,61,65,66</sup> Moreover, strain rates applied in simulations are very high, usually  $\sim 10^8 \text{ s}^{-1}$ ,<sup>60,61</sup> which is much higher than those of  $\sim 10^{-4} \text{ s}^{-1}$  applied in experiments.<sup>43,44,57</sup> Therefore, experimentation at the nanoscale is required to confirm the computational results and correct methodological artifacts. With the progressive development of advanced microscopy techniques including *in-situ* deformation conducted using the atomic force microscope (AFM), within the scanning electron microscope (SEM), or transmission electron microscope (TEM), a number of *in-situ* nanomechanical testing modes of NWs have been developed, including bending,<sup>29,40,42,45,67</sup> resonance,<sup>41,68–70</sup> uniaxial loading,<sup>46,51,71–73</sup> and nanoindentation.<sup>74–76</sup> Nevertheless, owing to the small dimensions of NWs, accurate mechanical characterization of NWs is still a challenge to many existing testing and measurement techniques. Manipulation and installation of individual NWs with such small sizes in a test setup are badly tough tasks, and the force applied to a NW may be too small to be precisely detected by existing testing facilities. Therefore, a combined experimental and theoretical methodology should be used to harvest a comprehensive understanding of mechanical behavior of NWs. Up to date, extensive researches in the field of mechanical behavior of NWs have been conducted to propel nanoscience and nanotechnology forward. However, the remarkable challenge in nanoscale experiments and misinterpretation of data still exist. In this review paper, we will comprehensively summarize the current experimental investigations of mechanical behaviors of metallic and semiconductor NWs and propose methods to overcome the challenges and misinterpretation of nanomechanical testing of NWs. As semiconductor materials always have covalent/ionic bonds, which are the characteristic of ceramics, “ceramic NWs” will be used to include

“semiconductor NWs” thereafter. Different from several review papers on the deformation of small-sized materials systems such as micro or sub-micrometer pillars produced by the focused ion beam (FIB) technique,<sup>33,34,64</sup> this review focuses on NWs without artificial defect introduced during sample preparation processes.

This review article is organized into the following sections. Section II reviews the development of the experimental techniques in the past two decades for quantifying the mechanical properties and understanding the deformation mechanisms of NWs. Section III discusses the mechanical behaviors of NWs including Young’s modulus, elastic strain limit, Poisson’s ratio, anelasticity, strength, plasticity, and fatigue properties. Section IV surveys the effects of planar defects, including stacking faults (SFs) and twins, on the mechanical behavior of NWs. Section V gives a brief summary and outlook for future research directions.

## II. EXPERIMENTAL TECHNIQUES FOR NANOMECHANICAL TESTING

Quantitative characterization of the mechanical behavior of NWs is quite challenging due to the difficulty of experimental setup and the requirement of force-displacement ( $F-d$ ) measurement with high force and displacement accuracy. With the progress of experimental instruments, several nanomechanical testing techniques have been developed to investigate the mechanical properties of NWs. These techniques differ from each other, which can be categorized in different ways based on the mechanical properties measured and the platforms used for the nanomechanical characterization. For example, since all nanomechanical characterizations of NWs were conducted by recourse to the microscopes due to the small dimensions of NWs, the testing methods can be grouped into AFM/nanoindentation testing and electron microscopy testing. In addition, depending on the condition if simultaneous mechanical testing and structural characterization can be conducted or not, the methods are regarded as *in-situ* or *ex-situ* ones. Here, we categorize and review the existing techniques for nanomechanical characterization of NWs from the literature based on the loading modes, including bending, resonance, uniaxial loading, and nanoindentation.

### A. Bending

Considering the dimensional characteristics of NWs with the diameters of the order of 100 nm and the lengths of tens of microns, bending has been widely applied to characterize their mechanical behaviors. Bending tests of NWs can be performed in AFM, TEM, and SEM. There are two types of bending tests: (1) one end of individual NWs is fixed, the other end is free, and then a load is applied at the free end to bend the NWs and (2) both ends of individual NWs are fixed and the load is applied at the middle point of the NWs, which is termed as “three-point bending.”

According to the fabrication methods of NWs, the first type of bending test can be conducted in slightly different ways. For NWs that are epitaxially grown perpendicular to the substrate, one end of the NWs has already been fixed at

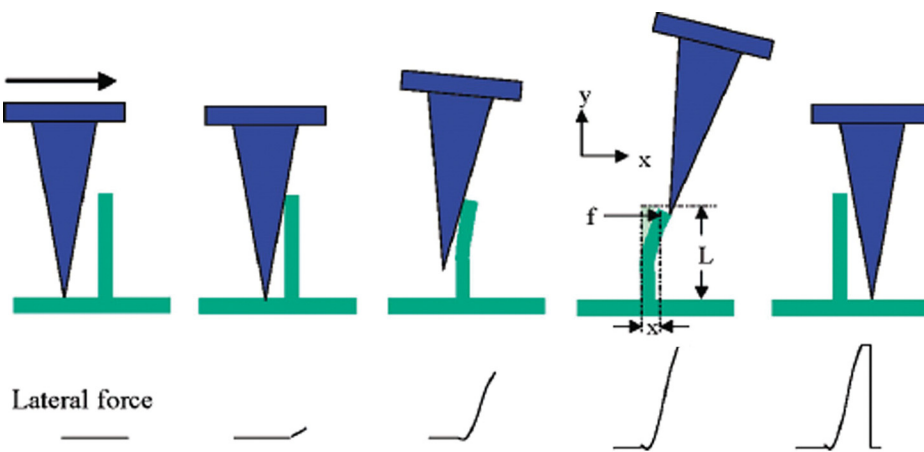


FIG. 1. A schematic diagram demonstrating a bending experiment of a NW using an AFM tip.<sup>77</sup> Reprinted with permission from Song *et al.*, Nano Lett. **5**, 1954 (2005).<sup>77</sup> Copyright 2005 American Chemical Society.

the substrate, the AFM probe (or cantilever) is used to bend the free end of the NWs through applying a lateral force perpendicular to the NW axis, as schematically illustrated in Fig. 1.<sup>77</sup> Both the bending force and bending distance can be recorded simultaneously through lateral force imaging and topographic imaging (feedback signal from the cantilever), respectively. The Young's modulus  $E$  of individual NWs is derived from the measured relationship between load and deflection using the following equation:<sup>77</sup>

$$E = \frac{FL^3}{3Ix}, \quad (1)$$

where  $F$  is the lateral force applied to the NW,  $I$  is the momentum of inertia of the NW ( $I = \pi R^4/4$ , where  $R$  is the radius of the bent NW curvature),  $x$  is the lateral deflection perpendicular to the NW at the loading point, and  $L$  is the length from the root of the NW to the loading point. This technique allows direct measurement of the mechanical properties of individual NWs without destructing or manipulating the sample.

For NWs that are randomly distributed on a flat substrate surface, the first step is to deposit a regular array of SiO<sub>2</sub> square pads to fix the randomly dispersed NWs onto the substrate through a shadow mask. An AFM is then used to locate and characterize the dimensions of protruding NWs. The NW protruding from the pads are tested by applying lateral load using the AFM cantilever tip. This method was first used to quantify the Young's modulus and fracture strength of SiC NWs.<sup>78</sup> In the past two decades, AFM is a major platform for the investigation of the mechanical behavior of NWs. While AFM-based testing techniques enable direct measurement of force as a function of displacement, from which the mechanical properties of NWs are extracted, the techniques are incapable of real-time imaging, which makes it difficult to interpret the  $F$ - $d$  relationships based on the details of the structural evolution during NW deformation processes.

By recourse to a special TEM sample holder equipped with AFM/nanoindentation systems, *in-situ* bending tests of NWs can be performed in TEM, allowing simultaneous mechanical testing and structural characterization. Figure 2(a) presents an example of this type of TEM holders that can be used to characterize the mechanical behavior of

individual NWs.<sup>79</sup> During the experimental process, a gold wire with NWs stuck at its tip is adhered to the piezo-driven mobile manipulator of the holder, which can move precisely towards the AFM tip to make contact between the AFM tip and a NW, as shown in Fig. 2(b). Bending force is applied via the nanoindentation tip to deform the NW. Young's

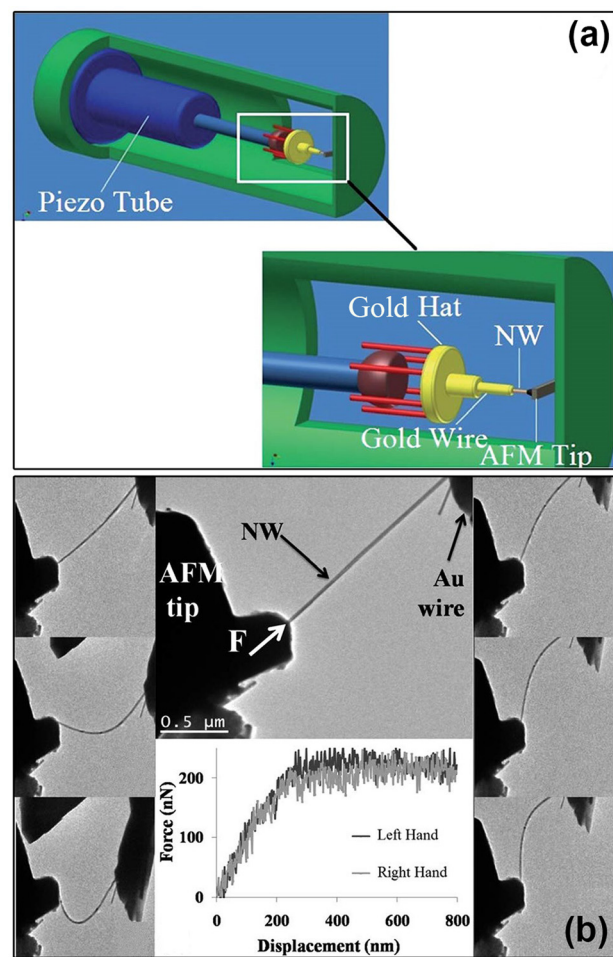


FIG. 2. (a) A schematic of an *in-situ* AFM-TEM holder used for mechanical measurements. (b) Experimental setup, leftward and rightward bending experiments of individual ZnTe NWs, and plots of the force-displacement of both the rightward and leftward bending of the NW.<sup>79</sup> Reprinted with permission from Davami *et al.*, Nanoscale **4**, 897 (2012). Copyright 2011 Royal Society of Chemistry.

modulus is calculated from the obtained  $F$ - $d$  curve, which is independent on the bending direction [Fig. 2(b)]. Thanks to the real-time high-resolution imaging capability of TEM, this method enables direct correlation of structures, individual structural evolution events, and mechanical responses of NWs at very high spatial and force resolutions.

Although some bending tests conducted in SEM do not provide any  $F$ - $d$  curve, the quantitative strength and strain values of NWs at fracture can still be calculated by direct observation using the elasticity theory. The fracture strain  $\varepsilon_f$  can be calculated from a simple beam theory using the following equation:<sup>45</sup>

$$\varepsilon_f = \frac{3D\delta}{2L^2}, \quad (2)$$

where  $D$  is the NW diameter,  $\delta$  is the deflection at the loading point, and  $L$  is the NW length measured from the root to the loading point. If the Young's modulus  $E$  is known, the fracture strength  $\sigma_f$  can be calculated by<sup>45</sup>

$$\sigma_f = \varepsilon_f E = \frac{3D\delta}{2L^2} E. \quad (3)$$

In addition, with three-dimensional (3D) finite-element analysis (FEA),<sup>40,42,45</sup> the stress/strain distribution in the NW cross-section can be derived. Therefore, the fracture strain  $\varepsilon_f$  of the NW equals to the maximum strain at the root of the NW and can be obtained directly from the contour plot of the strain distribution of the NW just before fracture.

The three-point-bending method,<sup>29,47,80–84</sup> in which a force perpendicular to the NW axis is applied at the middle point of a double-clamped NW, has also been used in AFM to measure the mechanical properties of individual NWs. Figure 3(a) exhibits the schematic illustration of a three-point-bending test process using an AFM tip. This method involved suspending a NW over a fabricated trench, clamping the NW across the trench using a deposition technique and measuring their response under lateral load from the AFM tip. Figure 3(b) presents an SEM image of a suspended Au NW with its two ends clamped at the trench edges by electron-beam-induced deposition of Pt and lateral force

applied by an AFM probe to the midspan of the double-clamped NW for the bending test. The  $F$ - $d$  curve was recorded during the test, as shown in Fig. 3(c). Curve 1 revealed that the NW was elastically loaded as detected from the linear slope and reversible loading and unloading, while curve 2 and 3 showed the same initial linear region followed by plastic deformation. The linear-elastic F-d curves are consistent with the beam bending theory and can be applied to analyse the mechanical properties of NWs. For example, the Young's modulus of individual NWs can be determined using the following equation:<sup>29</sup>

$$E = \frac{FL^3}{192I\delta}, \quad (4)$$

where  $\delta$  is the deflection at the midspan of the NW induced by the applied load  $F$  and  $I$  and  $L$  are the moment of inertia ( $I = \pi R^4/4$ , where  $R$  is the radius of the bent NW curvature) and the suspended length of the NW, respectively. In addition to Young's modulus, the yield strength  $\sigma_y$  can also be obtained from this method:  $\sigma_y = F_y/A$ , where  $F_y$  is the force obtained from the  $F$ - $d$  curve at the yield point, after which point, the slope of the curve becomes different from that of the initial linear elastic region, and  $A$  is the cross-sectional area of the NW. This method has also been applied to the mechanical property measurement of other materials, including Si<sup>80</sup> and SiO<sub>2</sub><sup>82</sup> NWs.

Although the above-mentioned methods enable direct measurement of the mechanical properties of NWs subjected to bending, they do not provide real-time observation of defects nucleation and propagation that is crucial to comprehend the deformation behaviors of NWs at the atomic scale. Han *et al.* creatively developed a technique that enables *in-situ* observation of the deformation process of individual NWs at the atomic-level resolution.<sup>43,44,49,55,67,85,86</sup> In this technique, NWs are sonicated off the substrate, dispersed in ethanol, and then deposited on a TEM grid with a broken colloidal/carbon supporting film on the Cu grid as schematically shown in Fig. 4(a). When the broken colloidal/carbon film is irradiated/heated by the electron beam, it undergoes shrinkage that applies tensile [Figs. 4(b) and 4(c)] or bending

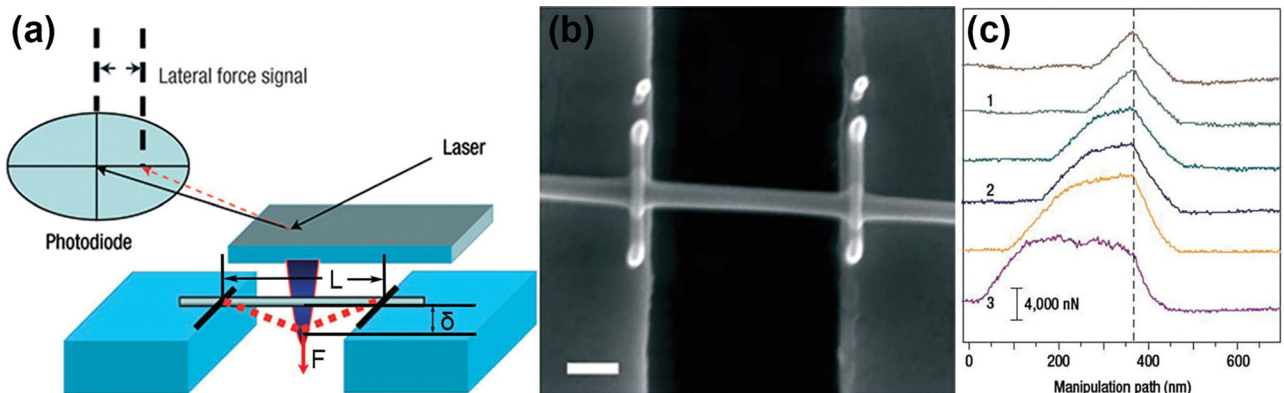
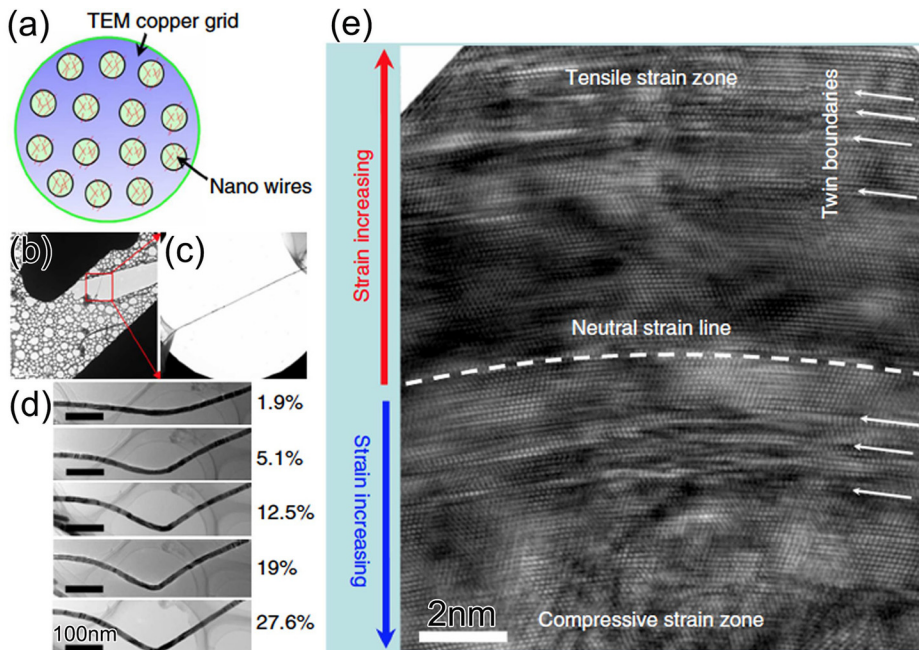


FIG. 3. (a) A schematic illustration of a three-point-bending test process using an AFM tip. (b) An SEM image of the Au NW fixed by electron-beam-induced deposition of Pt lines. (c)  $F$ - $d$  curves recorded during consecutive manipulation by AFM tip-induced lateral bending of a 200-nm Au NW. The scale bars are 500 nm.<sup>29</sup> Reprinted with permission from Wu *et al.*, Nat. Mater. 4, 525 (2005). Copyright 2005 Nature Publishing Group.

force [Fig. 4(d)] to individual NWs deposited on it. The advantage of this types of experiments is that they can be conducted in a high-resolution TEM (HRTEM) using a double-tilted holder so that individual NWs can be tilted to a specific zone axis for HRTEM imaging to reveal the atomic-scale deformation mechanisms, such as unusual large plasticity in ceramic NWs<sup>44,49,55,85</sup> and continuous and reversible lattice deformation beyond the elastic limit of nanotwin-structured Ni NWs [see Fig. 4(e)].<sup>67</sup>

Another way to investigate the atomic-scale mechanism of NWs' bending deformation is by deforming a NW in SEM/FIB using a manipulator, keeping the deformed status by fixing the both ends of the bent NW on the TEM grid, and then moving the NW to TEM for HRTEM observation.<sup>87</sup> The bending strain is the NW is controllable. The atomic structure of the NW before, during, and after bending can be observed using HRTEM.

Generally, AFM-based bending experiments can be readily performed to provide quantitative measurement of mechanical properties of NWs including their Young's modulus, yield and fracture strengths, and fracture strain because no complicated specimen preparation is needed and the testing can be completed in short time. Although it is relatively difficult to conduct quantitative bending tests of NWs in SEM and TEM, the atomic-scale plasticity including the nucleation and propagation of defects can be directly visualized using *in-situ* and *ex-situ* HRTEM observations. However, the stress status of NWs under bending conditions is very complicated, with one lateral side under compression and the other side under tension. This makes it difficult to build a direct relationship between deformation mechanisms and mechanical properties of NWs. The measurement of the curvature of the bend NW in TEM or SEM could be a possible source that affects the accuracy of the results. The curvature is measured from the two-dimensional projection of a three-dimensional curvature of a NW, and this may lead to underestimation of the bending strain.



## B. Resonance

The resonance method is based on the natural resonant vibration of a single cantilevered NW that is excited by thermal, electrostatic, or mechanical methods.<sup>88</sup> This technique was first applied to characterize the mechanical behaviors of individual carbon nanotubes<sup>89</sup> and has also been applied to NWs.<sup>41,68–70,90,91</sup> Compared with the resonance induced by thermal and mechanical excitation, the electric-field-induced resonance excitation can be readily controllable by using an alternating current (AC). As shown in Fig. 5,<sup>41,88</sup> the application of a frequency tunable AC voltage across the tungsten tip and the counter electrode drives the NW to vibrate mechanically, from which the resonance frequency is measured. The resonance frequency is determined from the frequency–amplitude relationship. When the frequency of the driving voltage is equal to the resonant frequency, the NW vibrates with the largest amplitude. According to the Euler–Bernoulli analysis of a cantilevered beam,<sup>92</sup> the resonance frequency  $f_n$  of the NW depends on the Young's modulus  $E$  of the NW

$$f_n = \frac{\beta_n^2 D}{2\pi L^2} \sqrt{\frac{E}{16\rho}}, \quad (5)$$

where  $\beta_n$  is a constant for the  $n$ th harmonic mode,  $D$  and  $L$  are the diameter and the length of the NW, respectively, and  $\rho$  is the material density. When the aspect ratio  $L/D$  of the NW is below  $\sim 200$ , usually, only the fundamental mode of vibration is excited, in which  $\beta_0 = 1.875$ . This equation is used to extract the Young's modulus of individual NWs by measuring their resonance frequencies and dimensions. Thanks to their powerful *in-situ* imaging capability, TEM and SEM are excellent platforms for resonance experiments, which allow accurate measurements of the dimensions of NWs and direct monitoring of the resonance. In addition, AFM has also been used for resonance experiments.<sup>93</sup>

Most recently, an *in-situ* TEM electric-field-induced resonance method was used to investigate the fatigue behavior

FIG. 4. (a) NWs scattering on a TEM Cu grid. (b) and (c) TEM images showing the tensile deformation. (d) A series of TEM images showing bending process of a Ni NW on a broken colloidal/carbon film when the film shrank as a result of the electron-beam illumination. (e) Atomic-scale image of the bent Ni NW.<sup>67</sup> Reprinted with permission from Wang *et al.*, Nat. Commun. **4**, 2413 (2013). Copyright 2013 Nature Publishing Group.

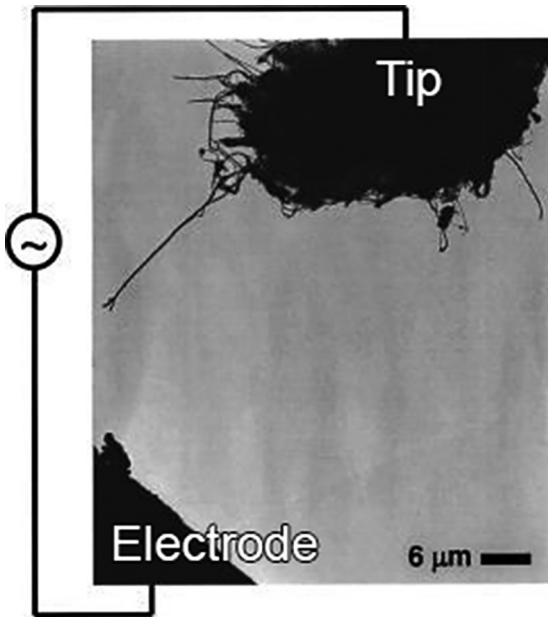


FIG. 5. A TEM image showing the resonance of a single NW. The NW is actuated by applying an AC signal between the sample and the ground electrode.<sup>88</sup> Reprinted with permission from Appl. Phys. Lett. **85**, 4328 (2004). Copyright 2004 AIP Publishing LLC.

of NWs.<sup>94,95</sup> Using the same method discussed above, loading cycles are applied to a NW by a periodic electrostatic force driven at the NW's resonance frequency. Fatigue behavior can be directly monitored in TEM so that fracture can be immediately captured. The number of loading cycles can be determined from the resonance frequency multiplied by the elapsed time. While mechanical characterization of NWs using the resonance method is simple and has been widely used, the only mechanical property that can be extracted from the resonance method is the Young's modulus.

### C. Uniaxial loading

Compared with other deformation modes, uniaxial loading is the most straightforward mechanical testing method. However, due to the difficulty in manipulating small objects such as NWs, uniaxial-loading mechanical characterization of individual NWs is not an easy task. Since uniaxial loading tests can provide a large spectrum of mechanical properties in the regions of both elastic and plastic deformation and the experimental results can be readily interpreted, several

techniques have been developed to perform uniaxial tensile and compression loading of individual NWs in SEM or TEM.

Figure 6(a) presents an SEM image taken during the tensile test for a NW with a diameter of 20 nm, while the inset at the lower left part presents a magnified image of the NW, and the SEM image of Fig. 6(b) shows the fracture of the NW.<sup>51</sup> It is clear that one end of the NW was clamped to the tungsten tip of a nanomanipulator and the other end was jointed on an AFM cantilever using electron-beam-induced deposition. The precision movement of the nanomanipulator imposes a tensile force on the NW and the AFM cantilever works as the load sensor. A series of SEM images can be taken during tensile process, from which elongation can be directly measured for plotting the stress-strain curve. Based on the highly accurate stress-strain curves, the Young's modulus, yield strength, fracture strength, elastic strain, and ductility of individual NWs can be extracted. This technique has been successfully applied for quantitative stress-strain measurements of Au,<sup>96</sup> Si,<sup>50</sup> and ZnO<sup>51</sup> NWs.

The same experimental setup for tensile testing can also be used for compression tests of individual NWs in SEM through moving the nanomanipulator towards the AFM cantilever to apply compressive load to the NWs.<sup>51</sup> During the compression, buckling occurs [Fig. 6(c)] due to the large ratios of length over diameter. The Young's modulus  $E$  can be computed from the Euler's formula<sup>97</sup>

$$E = \frac{P_{cr}L_e^2}{\pi^2 I}, \quad (6)$$

where  $P_{cr}$  is the critical buckling load,  $I$  is the moment of inertia of the NW ( $I = \pi R^4/4$ , where  $R$  is the radius of the NW), and  $L_e$  is the effective length ( $L_e = 0.5L$  for the fixed-fixed boundary condition, in which both ends of the NW are fixed without any translational or rotational motion, where  $L$  is the actual length of the NW).

Deforming a NW in SEM via an AFM probe or nanomanipulator<sup>96</sup> enables direct real-time observation of the morphological changes of the NWs during the entire loading process. The large chamber size in SEM makes it easy to manipulate the NW deformation processes. However, it is impossible to reveal the structural evolution and deformation mechanisms of NWs during *in-situ* testing in SEM. This problem can be overcome by conducting *in-situ* experiments in TEM.

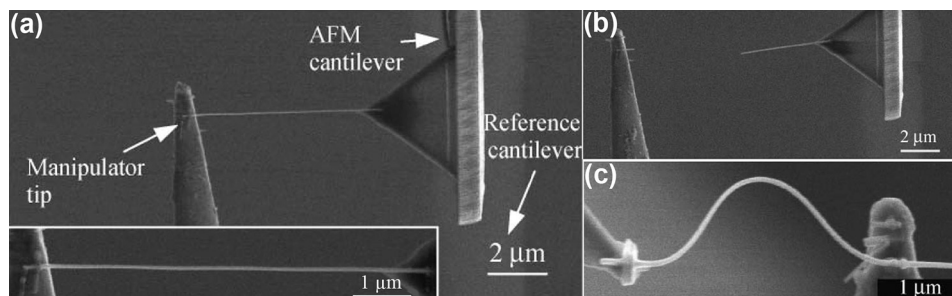


FIG. 6. (a) An SEM image taken during the tensile test for a NW. Inset at the lower left corner is an enlarged SEM image of the NW. (b) An SEM image of a fracture NW subjected to tensile deformation. (c) An SEM images showing buckling of the NW induced by the compressive load.<sup>51</sup> Reprinted with permission from Xu *et al.*, Nano Res. **3**, 271 (2010). Copyright 2010 Tsinghua University Press and Springer-Verlag Berlin Heidelberg.

Recently, *in-situ* deformation TEM has been progressively developed. The Hysitron PicoIndenter<sup>®</sup> and NanoFactory holders have been the most commonly used commercial products for *in-situ* TEM tensile, compression, and bending tests.<sup>54,58,98–107</sup> Figure 7(a) presents an image of the Hysitron PI 95 TEM PicoIndenter and Fig. 7(b) presents a schematic diagram of the working mechanism of a compression test of a NW using the PicoIndenter. To perform a uniaxial compression test of individual NWs using this holder, a substrate with vertically aligned NWs is carefully attached to the mount so that the NW axial direction is perpendicular to the flat front surface of the piezo-driven diamond flat punch. In response to a gradually increased compressive load, buckling of the NW occurs before fracture. The fracture strength and critical buckling load of the NW can be easily obtained from the simultaneously measured  $F$ - $d$  curve. Also, the Young's modulus can be calculated from the critical buckling load using Eq. (6).

*In-situ* tensile testing in the TEM can be accomplished by coupling the PicoIndenter with a push-to-pull (PTP) device. The PTP device has a specially designed structure, as presented in Fig. 8. There is a mobile part and a fixed part in the PTP. A NW is fixed at the two ends of the gap indicated in Fig. 8 by a circle between the mobile and fixed parts. When the mobile part is pushed towards the fixed part, the gap expands so that the compression load is converted into a tensile load that is applied to the NW bridging the gap. This device has been widely used in a TEM to study the mechanical behaviors of various kinds of NWs, such as tensile strength of submicron-sized metallic glass wires,<sup>109</sup> the elastic properties and strain-induced phase transformation of individual VO<sub>2</sub> NWs,<sup>102</sup> and dislocation activities in Mo alloy nanofibers.<sup>110</sup>

Another popular device for tensile deformation of individual NWs is a microelectromechanical systems (MEMS)-based nanomechanical testing system, as shown in Fig. 9. The MEMS offers force-displacement measurements with high spatial and force accuracy of 1 nm and 12 nN, respectively.<sup>111</sup>

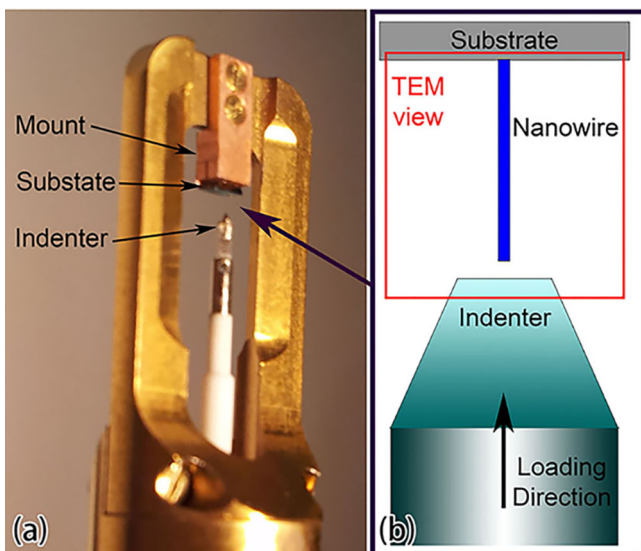


FIG. 7. (a) An image of a Hysitron PI 95 TEM PicoIndenter. (b) A schematic diagram of a compression test of a NW using the Hysitron PI 95 TEM PicoIndenter.<sup>108</sup>

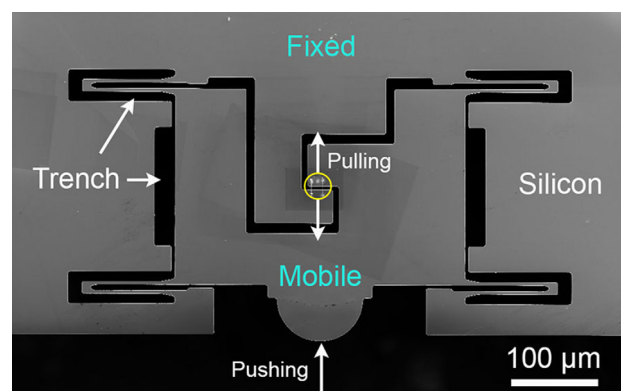


FIG. 8. An SEM image of a PTP device. The black areas are empty space and the dark grey areas are silicon. When the device is pushed on the semi-circle end of the mobile part (arrow at bottom), the gap indicated by a yellow circle expands and converts compressive force into tensile force.

The high accuracy is achieved by controlling a thermal actuator for displacement and a capacitive load sensor. In fact, these specially designed apparatuses for nano-tensile testing have also been widely used in SEM.<sup>51,112–114</sup> Although these types of specially designed *in-situ* straining TEM holders can provide quantitative stress-strain data, it is very difficult to use them for two-dimensional HRTEM imaging for the investigation of atomic-scale deformation mechanisms because the holders are usually single-tilt, making it very difficult to tilt NW samples to a specific crystallographic zone axis for HRTEM imaging.

Han *et al.* have pioneered a method that allows two-dimensional HRTEM imaging during *in-situ* uniaxial tensile deformation with controllable strain rate in TEM, which apparently increases the space resolution by three orders of magnitude.<sup>46,56,115–119</sup> The working mechanism of the method is demonstrated in Fig. 10. A specimen, which can be a NW, is attached to the edges of the trench between two bimetallic strips made of two materials that have different thermal expansion coefficients. When the strips are heated in a double-tilt TEM specimen holder with the heating capability, the bimetallic strips bend slowly in opposite directions, pulling the sample with an adjustable strain rate that is controlled by the temperature of the heating stage. Different from other techniques based on single-tilt holder relying on

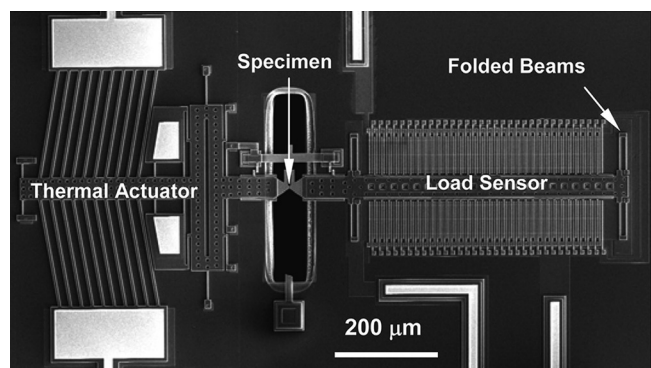


FIG. 9. MEMS-based nanomechanical testing system including actuator, load sensor, and specimen.<sup>73</sup> Reprinted with permission from Agrawal *et al.*, Nano Lett. 8, 3668 (2008). Copyright 2008 American Chemical Society.

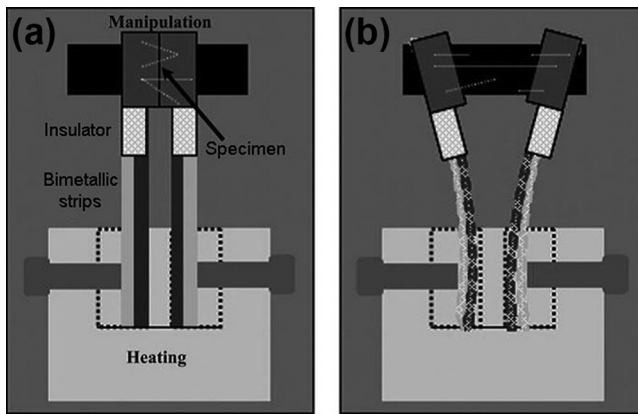


FIG. 10. An illustration of the NW tensile testing technique using bimetallic strips. (a) Prior to the tensile test. (b) During the tensile test.<sup>46</sup> Reprinted with permission from Zhang *et al.*, Adv. Funct. Mater. **17**, 3435 (2007). Copyright 2007 John Wiley and Sons.

the burdensome manipulation of NWs with a proper crystallographic orientation for HRTEM imaging, this creative *in-situ* technique is the only method at present that takes advantage of the double-tilt holder to enable real-time investigation of tensile deformation mechanisms at the atomic resolution. The technique has opened up the new research area of the atomic-scale deformation dynamics of material,<sup>43,44,46,49,55,56,67,85,115–122</sup> which enriches and enlivens our understanding of deformation mechanisms of advanced materials.

Although significant progresses in mechanical characterization of individual NWs under uniaxial tension have been made, experiments in this area are still highly challenging since significant efforts are needed for specimen preparation due to the requirement of clamping NW samples to the testing stage and since it is very difficult to properly align the NW axial direction with the loading direction. Characterization of NWs using this method requires the meticulous experimental skills and a great deal more time than other methods. However, the stress state of the NWs under uniaxial tension is very simple, leading to easy interpretation of the measured mechanical data and deformation mechanisms.

#### D. Nanoindentation

One of the most commonly used techniques for the investigation of mechanical properties of materials is nanoindentation. In this method, a nanometer-sized hard tip or nanoindenter is pressed into a sample by applying small force to measure its Young's modulus and hardness. Nanoindentation has been widely used in AFM for mechanical characterization of nanobelts<sup>76,123,124</sup> and NWs.<sup>74–76</sup> For nanoindentation of individual NWs, a NW is lying flat on the substrate, and both ends of the NW are fixed on the substrate by electron-beam-induced deposition to prevent the NW from moving around. Using an AFM tip to perform indentation is likely to cause slip and friction between the AFM tip and the sample surface during the indentation because the AFM tip cannot be perpendicular to the surface of circular-shaped NWs. This shortcoming has been solved by using a Berkovich (three-sided pyramidal diamond)

indenter to perform the imaging and indentations. Hardness and Young's modulus were extracted from the  $F$ - $d$  curve obtained by nanoindentation. Nanoindentation hardness  $H$  can be calculated from the following equation:<sup>74</sup>

$$H = \frac{P_{max}}{A}, \quad (7)$$

where  $P_{max}$  is the indentation load, which is the peak load from the  $F$ - $d$  curve, and  $A$  is the projected contact area of the indentation. The Young's modulus of the NW can then be obtained from the expression of  $E_r$ <sup>74</sup>

$$\frac{1}{E_r} = \frac{1 - \nu^2}{E} + \frac{1 - \nu_i^2}{E_i}, \quad (8)$$

where  $E_r$  is the reduced elastic modulus that accounts for the fact that elastic deformation occurs in both the sample and the indenter, while  $E$  and  $E_i$  are the elastic moduli, and  $\nu$  and  $\nu_i$  are the Poisson's ratio for the sample and the indenter, respectively. Poisson's ratio of the sample is usually obtained from literature or simply set to be the bulk value. The following equation can be applied to determine the  $E_r$  that accounts for the fact that elastic deformation occurs in both the sample and the indenter:<sup>74</sup>

$$S = 2\beta\sqrt{\frac{A}{\pi}E_r}, \quad (9)$$

where  $S$  is the unloading stiffness that can be obtained from the slope of the initial portion of the unloading curve, and  $\beta$  is a constant that depends on the geometry of the indenter ( $\beta = 1.034$  for a Berkovich indenter). Although this method is quite simple, it is difficult to eliminate the friction force from the substrate.

### III. MECHANICAL BEHAVIORS OF NWs

#### A. Young's modulus

Young's modulus or elastic modulus is a measure of the stiffness of a material and is quantified as the ratio of stress to strain, both along the same axis, for elastic deformation. At the atomic scale, the magnitude of the Young's modulus is a measure of strength of interatomic forces between adjacent atoms or ions that vary with the type of bonding in materials.<sup>125</sup> For bulk materials, Young's modulus is an intrinsic property of materials and is independent of the dimensions of the materials. Differently, NWs have a large surface-to-volume ratio and surface atoms play a significant role in determining their properties. The reduced coordinate number of atoms at the surface will lead to either softening or stiffening elastically relative to the corresponding bulk materials, depending on the competition between the softening due to the loss of bonding neighbours and the stiffening gained from electron redistribution at the surface.<sup>126</sup> As a result, the Young's modulus of the NWs generally varies from their bulk counterparts and is size-dependent.

The size dependence of Young's modulus is important for the applications of NWs and, therefore, has attracted significant attention from researchers. However, results on the

Young's modulus of NWs have been significantly scattered. Taking ceramic NWs, for example, it was reported that the Young's modulus of ZnO NWs with diameters ranging from 18 to 304 nm<sup>47</sup> is close to the bulk value ( $\sim$ 140 GPa) calculated from the elastic constant.<sup>69</sup> However, the Young's modulus of ZnO NWs with diameters of  $\sim$ 45 nm measured using AFM lateral bending experiments was  $29 \pm 8$  GPa,<sup>77</sup> which is significantly lower than the bulk value; a much larger Young's modulus of 220 GPa for ZnO NWs with a diameter of 17 nm was obtained from electric-field-induced resonance measurement.<sup>69</sup> Similarly, the measured elastic properties of metallic NWs, e.g., Au NWs, were also scattered and controversial. The average Young's modulus of Au NWs with diameter ranging from 40 to 250 nm measured from AFM bending experiments was  $70 \pm 11$  GPa,<sup>29,30</sup> which is close to the value of bulk Au (78 GPa).<sup>125</sup> Resonance experiments demonstrated that the Young's modulus of single crystalline  $\langle 100 \rangle$  Au NWs was  $31 \pm 1$  GPa, which is lower than the bulk value of 42 GPa along the  $\langle 100 \rangle$  directions.<sup>127</sup> A much larger Young's modulus of 139 GPa for  $\langle 100 \rangle$  Au NWs with a diameter of 2 nm was obtained from atomistic simulations.<sup>128</sup> The Young's modulus of  $\langle 111 \rangle$  Au NWs along the axial direction calculated from atomic simulations was also found higher than the bulk value of Au along  $\langle 111 \rangle$ .<sup>129</sup>

The sources that lead to the discrepancy in the Young's modulus of NWs are not clear, which could include experimental errors and structural variations. Experimental errors could be improved by eliminating experimental uncertainty in instrument calibration, mounting of NWs, and measurement of NW dimensions. Loading misalignment of NWs, which is usually unavoidable and ignored in mechanical property testing of NWs,<sup>130</sup> can lead to underestimation of the critical buckling load and tensile fracture strength, which has been confirmed using *in-situ* TEM compression tests and FEA, respectively, as illustrated in Figs. 11(a) and 11(b). Most epitaxially grown NWs are tapered rather than straight-edged because NW bases are grown first and hence are exposed to reactants for greater length of time than the later grown tips.<sup>17</sup> Ignoring the NW tapering during the data analysis of NW tensile or compression tests results in inaccuracy of the measured Young's modulus because an inaccurate

cross-sectional area of the NW is used.<sup>130</sup> Figure 11(c) presents the results of FEA showing the effects of neglecting taping angle of NWs on the critical buckling load of compression tests. Apart from the experimental inaccuracy, loading methods (tension, bending, or resonance) may yield different values of Young's modulus of NWs. Because NW surface carries more stress in flexural-loading conditions (i.e., resonance and bending) than in uniaxial loading conditions, the surface has a greater effect on the Young's modulus of NWs under resonance and bending than under tension. This hypothesis has been confirmed by the atomistic studies, showing that the surface effect during bending was six times than that under tension.<sup>32,131</sup> Using *in-situ* tensile and compression testing, the Young's modulus of ZnO NWs extracted from compression tests are much higher than that obtained by tensile tests.<sup>51</sup> In addition, the NW samples used in different studies may have different defect densities and surface roughness. Some NWs have core-shell structures with a native oxide layer but some do not. Therefore, structural information is also important for understanding these discrepancies. Combined detailed structural characterization at the atomic scale and careful mechanical testing would provide more information on the sources of the discrepancy.

Although scattering of measured Young's modulus of NWs exists, most studies supported the conclusion that the Young's modulus of NWs is a function of their diameters.<sup>45,69,73,132,133</sup> For example, the Young's modulus of ZnO NWs increases from 140 to 210 GPa when the diameter decreases from 550 to 17 nm [Fig. 12(a)],<sup>69</sup> while the same trend on the size effect on Young's modulus has also been reported in GaAs NWs [Fig. 12(b)].<sup>54</sup> It is well accepted that the size-dependency of the Young's modulus of NWs stems from the reconstruction of their surface structure, including surface atoms rearrangement to remove the tangling bonds<sup>51,69,73,132,133</sup> and formation of surface native oxide layer,<sup>54,72</sup> and the large surface-to-volume ratios of NWs result in significant increase in the contribution of the surface reconstruction to the overall mechanical properties of the NWs. The difference between the Young's moduli on the surface and in the bulk plays increasingly crucial roles in the Young's modulus of NWs by decreasing their diameters. Chen *et al.* proposed a core-shell model to explain the size

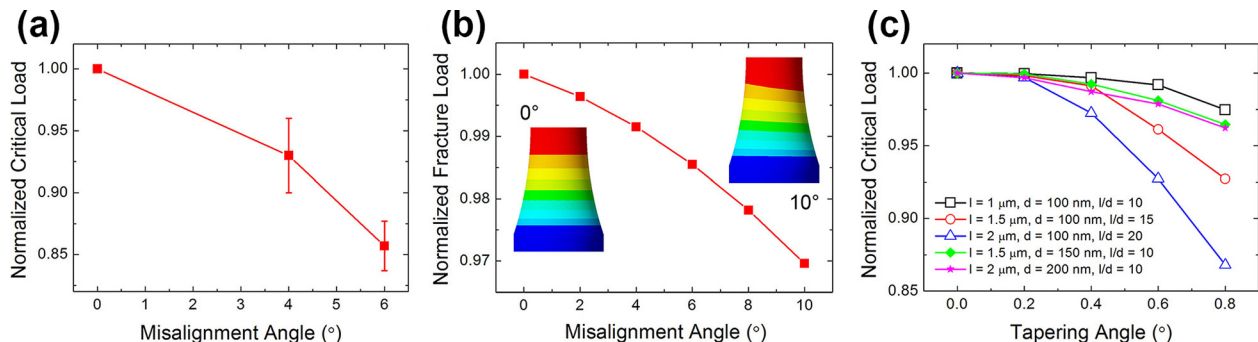


FIG. 11. (a) The effects of misalignment angle of loading on the normalized critical buckling load of cylindrical NWs under compression. (b) The effects of loading misalignment angle on the normalized fracture load of a cylindrical NW with a diameter of 100 nm and a length of 1.5  $\mu\text{m}$  under tension. The insets are the contour plot of maximum principal stress distribution at one end of a cylindrical NW under uniaxial tension and 10°-misaligned tension. (c) The effect of tapering angle on the normalized critical buckling load of tapered NWs with different slenderness ratios under uniaxial compression.<sup>130</sup> Reprinted with permission from Chen *et al.*, Nanotechnology 26, 435704 (2015). Copyright 2015 IOP Publishing Ltd.

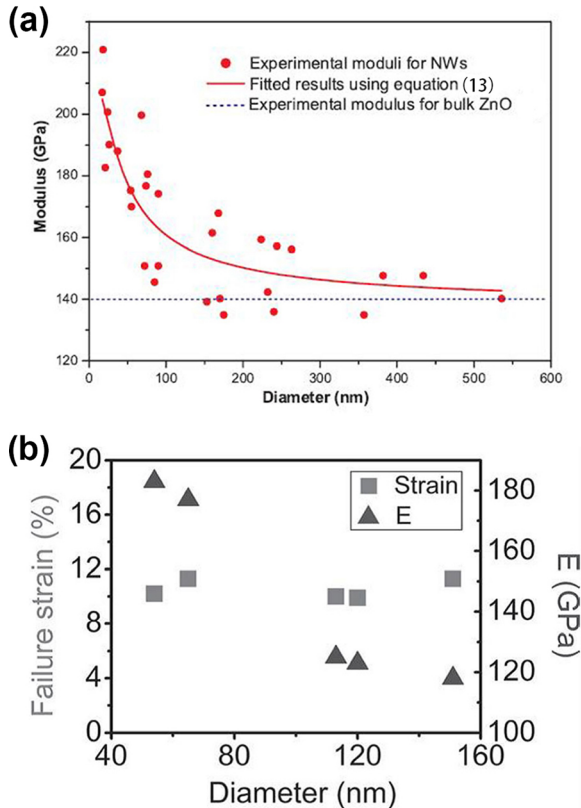


FIG. 12. The effect of the NW diameter on the Young's modulus of ceramic NWs. (a) Bending experimental results (red dots) and a fitted curve (the solid line) using a core–shell composite model for [0001] oriented ZnO NWs. The blue dashed line indicates the Young's modulus of bulk ZnO.<sup>69</sup> Reprinted with permission from Chen *et al.*, Phys. Rev. Lett. **96**, 075505 (2006). Copyright 2006 American Physical Society. (b) Compression experimental results (solid triangles) for GaAs NWs. The elastic strain at failure (solid squares) as a function of the NW diameter is also presented.<sup>54</sup> Reprinted with permission from Wang *et al.*, Adv. Mater. **23**, 1356 (2011). Copyright 2011 John Wiley and Sons.

dependence of Young's modulus ( $E$ ) of ZnO NWs. By assuming a NW with a diameter  $D$  having a core–shell structure composed of a core with modulus ( $E_0$ ) of the bulk material and a surface shell layer with constant thickness ( $r_s$ ) and a surface modulus ( $E_s$ ), the core–shell model can be expressed using the following equation:<sup>69</sup>

$$E = E_0 \left[ 1 + 8 \left( \frac{E_s}{E_0} - 1 \right) \left( \frac{r_s}{D} - 3 \frac{r_s^2}{D^2} + 4 \frac{r_s^3}{D^3} - 2 \frac{r_s^4}{D^4} \right) \right]. \quad (10)$$

This model has been successfully applied to explain the significant size effects of Young's modulus of various NWs, including ZnO and GaAs with either the cubic zinc-blende or the hexagonal wurtzite structures. In this model, the shell thickness is constant and independent on the whole diameters of NWs. However, a combined experimental/simulation study proposed that the effect of surface reconstruction rapidly decays beyond a certain number of atomic layers, and the number of these atomic layers increases by increasing the NW size.<sup>73</sup> It is suggested that the shell thickness remains  $\sim 15\%$  of the NW diameter, in contrast to the assumption made in the core–shell model.<sup>69</sup> Further investigations are needed to decode the underlying physical mechanism behind this model.

Based on a continuum-mechanics approach that describes the surface effect of NWs under tension and bending, a core–surface model<sup>32</sup> was established to calculate the effective Young's modulus ( $E$ ) of NWs with a diameter of  $D$ . In the model, a NW consists of a core with Young's modulus  $E_c$  and a surface with zero thickness and surface Young's modulus  $S$  (the unit is Pa·m). The effective Young's modulus  $E$  is given by the following equation:<sup>32</sup>

$$E = E_c + 4 \frac{S}{D} \quad \text{under tension and} \quad (11)$$

$$E = E_c + 8 \frac{S}{D} \quad \text{under bending.} \quad (12)$$

The surface-reconstruction mechanisms, including the core–shell and the core–surface models, have been experimentally confirmed and well accepted.<sup>38,51</sup> However, some atomistic studies explained the size effect through the bulk nonlinear elasticity, in which the residual tension-stiffened interior atomic layers were the main contributor to the size effect.<sup>134–136</sup> For example, it was found in Cu NWs that the axial compressive strain caused by surface stresses was large enough to induce a nonlinear elastic increase in the stiffness of bulk atoms, leading to an increase in the NW Young's modulus.<sup>136</sup> Recently, the anharmonic behaviors of Pd NWs provide strong support to this mechanism. The stress–strain curves of Pd NWs were characterized by linear elasticity at strain  $< 1\%$  and clear nonlinearity at larger elastic strains during *in-situ* tensile tests, while the Young's modulus prominently increased from 120 GPa for NWs larger than 100 nm to  $\sim 290$  GPa in the 33 nm NW.<sup>137</sup>

## B. Elastic strain

The elastic strain limit corresponds to the largest strain beyond which permanent and non-recoverable deformation, which is called plastic deformation, occurs. The theoretical elastic limit is the upper bound of the achievable elastic strain of a perfect, defect-free crystal. For most bulk metallic and ceramic materials under uniaxial loading, elastic deformation persists only to strains of  $\sim 0.5\%$  and  $\sim 0.1\%$ , respectively.<sup>125</sup> Elastic deformation is limited by the onset of pre-existing flaw induced crack propagation in ceramics or plastic yielding in metals, via, e.g., dislocation slip,<sup>125</sup> deformation twinning,<sup>138</sup> and/or phase transformation.<sup>139</sup> When the dimensions of materials are reduced to the micrometre or even nanometre regime, large elastic strains of  $\sim 2\%–10\%$  were observed in whiskers,<sup>30,31</sup> micro-pillars,<sup>103,140</sup> and NWs,<sup>54,56,72</sup> due to the limited sources of defects and the largely suppressed inelastic deformation under confining loading conditions in small volumes.

Large elastic strains in ceramic NWs have been widely reported (Table I).<sup>42–45,54,87,141,142</sup> For example, the elastic strain of SiC and Si NWs can be as high as  $\sim 2\%$ <sup>44</sup> and  $10\%$ ,<sup>142</sup> respectively, while the elastic strain of ZnO NWs measured by two research groups was  $7.7 \pm 0.8\%$ <sup>45</sup> and  $4\%-7\%$ .<sup>42</sup> Combined *in-situ* compression in TEM and FEA has been used to study the fracture strain of GaAs NWs (Fig. 13).<sup>54</sup> Extensive analysis of GaAs NWs with diameters in

TABLE I. Elastic, plastic, and fracture strain of ceramic NWs

Material	Loading	Fracture	Elastic strain (%)	Plastic strain (%)	Fracture strain (%)
GaAs	Compression	Brittle	11.3 <sup>54</sup>	—	11.3 <sup>54</sup>
Si	Tension	Brittle	10 <sup>142</sup>	—	10 <sup>142</sup>
ZnO	Bending	Brittle	7.7 <sup>45</sup>	—	7.7 <sup>45</sup>
ZnO	Tension	Brittle	6.1 <sup>51</sup>	—	6.1 <sup>51</sup>
GaAs	Bending	Ductile	3.16 <sup>87</sup>	0.99 <sup>87</sup>	4.15 <sup>87</sup>
SiC	Bending	Ductile	2 <sup>44</sup>	1.5 <sup>44</sup>	3.5 <sup>44</sup>
SiC	Tension	Ductile	8.9 <sup>141</sup>	46 <sup>141</sup>	54.9 <sup>141</sup>
Si	Bending	Ductile	—	—	21.5 <sup>49</sup>
Si	Tension	Ductile	—	—	125 <sup>43</sup>
Ge	Bending	Ductile	—	—	17 <sup>143</sup>
SiC	Tension	Ductile	—	—	200 <sup>46</sup>

the range of 50–150 nm showed that the fracture strains of these NWs were as high as 10%–11%, which is approximately 100 times larger than the bulk value. This indicates that the high elastic strain is independent of the NW diameter and could be an intrinsic material property. Bending experiments of GaAs NWs with a diameter of ~50 nm also revealed high elasticity with an elastic strain up to 3.16%.<sup>87</sup> In fact, for these brittle materials, cracks usually initiate at microscopic flaws or imperfections that exist at the surface and within the interior of the materials, which makes the material fracture at a strain far below its elastic limit. With the reduction of materials dimensions, the probability of the existence of a flaw in materials decreases. The fracture strain of ceramic NWs with no pre-existing defects is expected to be significantly higher than that of their bulk counterparts because of the absence of crack initiation by pre-existing flaws.

While the elastic strain of ceramic NWs is limited by the initiation of fracture, the elastic deformation of metallic NWs is limited by the initiation of dislocation activities.<sup>144</sup> The elastic strain can be accurately determined by analysing the variation in crystalline interplanar spacing before deformation and just before yielding through *in-situ* HRTEM or

selected area electron diffraction (SAED). Figures 14(a)–14(c) show the *in-situ* atomic-scale deformation process of a single crystalline Cu NW deformed along the [001] direction at different total strains, with the corresponding high-resolution fast Fourier transform images, from which the [001] interplanar spacing has been measured as shown in Fig. 14(d). For NWs with a large diameter, which is difficult or impossible to be imaged at the atomic resolution, the interplanar spacing was measured from the SAED patterns taken during the deformation. The results indicate that the achievable elastic strain in Cu NWs is size-dependent. The elastic strain increases from 1% to 7.2% as NW diameter decreasing from 1400 to 5.8 nm, as shown in Fig. 15. The maximum elastic strain (7.2%) approaches the theoretical elastic strain limit of Cu NWs and is so far the largest elastic strain under uniaxial tension.<sup>145</sup> The size dependence of the elastic strain is a result of the reduced dislocation sources with the decrease in the sample size. Limited dislocation sources delayed the onset of yielding and therefore increased the elastic deformation. *In-situ* tensile tests of ultrathin single crystalline Au NWs revealed their elastic strain of 4.5%.<sup>106</sup>

These results clearly demonstrate that NWs can sustain much higher elastic strain than their bulk counterparts due to

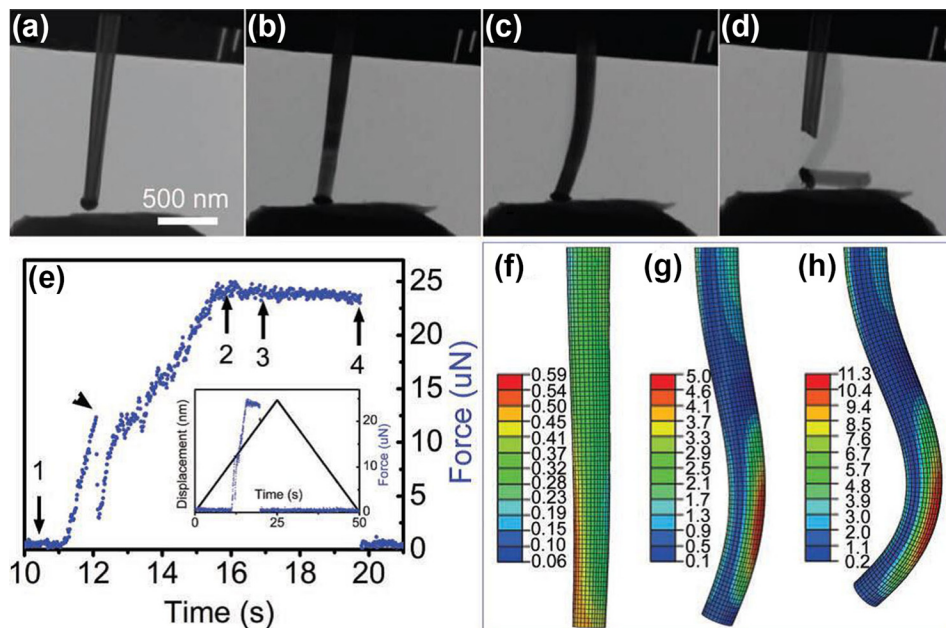


FIG. 13. (a)–(d) Snapshots of an *in-situ* compression test process of a GaAs NW. (e) A portion of the corresponding force–displacement–time curve, with the inset showing the complete curve of the whole testing process. Points 1–4 correspond to the images (a)–(d), respectively. (f)–(h) FEA models corresponding to the states in (b), (c), and (d), respectively.<sup>54</sup> Reprinted with permission from Wang *et al.*, Adv. Mater. 23, 1356 (2011). Copyright 2011 John Wiley and Sons.

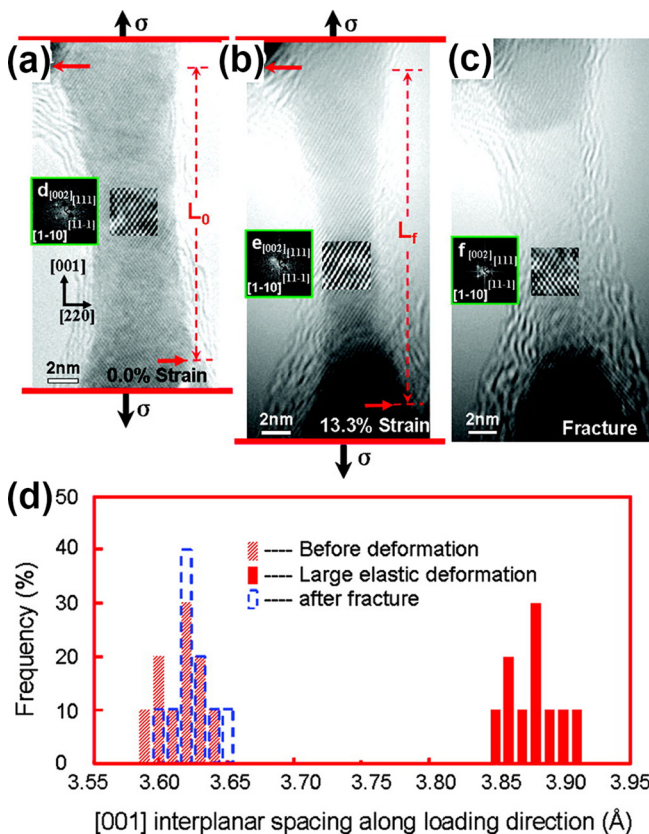


FIG. 14. (a)-(c) TEM, corresponding FFT, and IFFT images of a single crystalline Cu NW during *in-situ* atomic-scale deformation processes;<sup>56</sup> Reprinted with permission from Yue *et al.*, Nano Lett. **11**, 3151 (2011). Copyright 2011 American Chemical Society.

the diminished number of defects. The upper limit of lattice elastic strain is of significant interest in materials science since elastic straining alters the interatomic distance of neighboring atoms, which remarkably affects a legion of materials properties, including electronic structure,<sup>146–150</sup> thermal transport,<sup>151,152</sup> and optoelectronic<sup>153,154</sup> properties. The larger achievable elastic strain of NWs allows us to

apply far greater stress to manipulate and tune their physical and chemical properties than that imposed on bulk materials before plastic deformation or fracture. In fact, elastic-strain engineering has been widely applied to commercial semiconductor products. For example, strained silicon technology<sup>22,155,156</sup> has been widely used to improve the mobility of charged carriers (more than 50% improvement in response to tensile elastic strain of ~1%)<sup>156</sup> and electrical conductivity (a compressive elastic strain of 0.4% doubles the electrical conductivity).<sup>157</sup> Therefore, a window of opportunity has been opened to unveil the effects of these unexploited materials parameters and optimize the multiple functional properties of NWs.

### C. Poisson's ratio

Poisson's ratio is defined as the ratio  $\nu$  between transverse strain ( $\epsilon_t$ ) and longitudinal strain ( $\epsilon_l$ ) in the elastic loading direction.<sup>158</sup> As a macroscopic quantity, Poisson's ratio is highly related to the microscale properties of materials<sup>159</sup> and is an essential mechanical property in the research and development of modern materials. Poisson's ratios of materials are within a narrow numerical limit of 0.5 and -1.<sup>159</sup> Even for bulk materials, measurement of Poisson's ratio is difficult and the values are usually derived from the shear, bulk, or Young's modulus based on the elasticity theory.<sup>159</sup> Therefore, it is extremely challenging to determine the values of Poisson's ratio of NWs due to the difficulty of nanomechanical testing.

Investigation of Poisson ratio of NWs has been very limited, while the measured results are quite complicated when compared with their bulk counterparts. In a previous study on the effects of uniaxial elastic stress on the electronic properties of GaAs NW with a diameter of 40 nm, the energy shift of Raman peaks, which has a linear relationship with stress, was used to determine the strains in both of transverse and longitudinal directions. The Poisson ratio deduced from the strains was 0.16, which is smaller than that of bulk GaAs with a value of 0.186.<sup>160</sup> Recently, McCarthy *et al.* developed a general method, which involves mechanical manipulation and a simultaneous four-point electrical resistance measurement, to measure the Poisson ratio of wires at the macro-, micro-, and nano-scales.<sup>161</sup> Based on the relative change in resistance as a function of the normalized displacement per unit length during elastic deformation, Poisson's ratio of Ni NWs was determined to be ~0.317, close to the known bulk value of 0.31. However, the results of Ag NWs exhibit apparent scatter from 0.191 to 0.601, which are quite distinct from the bulk value of 0.37. The explanation about the variation of Poisson's ratio in the Ag NWs and the bulk counterpart is still an open question.

Poisson's ratio provides an essential metric to compare the performance of materials during elastic deformation.<sup>159</sup> This is fundamentally significant for NWs whose functionality can be elaborately tuned by elastic strain engineering. However, the relevance of Poisson's ratio is always underestimated by simply setting it as a fixed value. Besides the urgency of developing methods to accurately measure the Poisson's ratio of NWs, there are also several fundamental

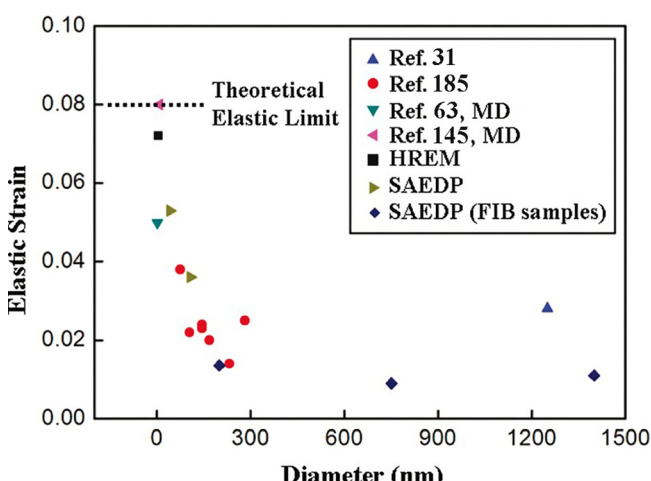


FIG. 15. Size dependence of elastic strain limit of single-crystalline Cu NWs and fibers.<sup>56</sup> Reprinted with permission from Yue *et al.*, Nano Lett. **11**, 3151 (2011). Copyright 2011 American Chemical Society.

questions to be answered, including (1) how the diameter of NWs affects the Poisson's ratio, (2) how the microstructure of NWs affects the Poisson's ratio, and (3) what the relationships between the Poisson's ratio and other mechanical properties of NWs are.

#### D. Anelasticity

In most materials, the elastic strain is completely recovered immediately after the applied load is retracted. In some materials, there also exists a time-dependent elastic-strain component and some finite time is required for complete recovery once a load is removed.<sup>125</sup> This phenomenon is known as anelasticity. The residual strain immediately after the release of the mechanical loading is called anelastic strain. Based on the time-dependent structural evolution, various underlying mechanisms of anelasticity have been proposed for different materials, including phase transformations,<sup>162</sup> reversible motion of twins,<sup>163,164</sup> grain reorientation,<sup>165</sup> cooperative motion of many atoms at grain boundaries,<sup>166</sup> and flow of free volume zones.<sup>167</sup> At the macroscopic scale, anelasticity is usually very small or negligible, especially in single-crystalline materials. It is well known that anelasticity always accompanies with the dissipation of internal mechanical energy. Therefore, materials with anelasticity have been widely applied in damping systems to reduce the noise for various industrial applications.<sup>168,169</sup> Investigations on the anelasticity of NWs can not only extend our understanding of deformation behaviour of the nanoscale materials but also open up the prospect of using ceramic NW materials for nanoscale energy damping applications.

Recently, it was found that single-crystalline ceramic NWs can exhibit anelastic behaviour with the anelastic strain up to four orders of magnitude larger than the largest anelastic strain ( $<10^{-6}$ ) observed in bulk materials and also with longer recovery time than bulk materials.<sup>170–172</sup> The anelastic behaviour in NWs was first reported in single crystalline GaAs NWs with small diameters (e.g., 25 nm).<sup>105</sup> The anelasticity in GaAs NWs is attributed to the amorphous surface layer and amorphous/crystalline interface. When the applied external stress was removed, the whole NW gradually returned to its original shape with a time delay since the amorphous layer holds back the crystal core resulting in a slow recovery. The anelastic behaviour was not observed in GaAs NWs with large diameters ( $>55$  nm) because the interfacial effect no longer dominates the mechanical behaviour of the NWs due to the significantly decreased surface-to-volume ratio. Further experimental and theoretical investigations are needed to uncover the detailed mechanism of anelasticity in GaAs NWs.

*In-situ* SEM bending tests of individual NWs revealed anelastic behaviour in single-crystalline ZnO and p-doped Si NWs and a different underlying mechanism was proposed.<sup>170</sup> Figure 16 presents a series of SEM images showing that after the removal of the bending load imposed on a ZnO NW, a large portion of the bending strain recovered instantaneously and the residual strain recovered gradually to its original shape over time. It was proposed that the origin of the anelasticity in ZnO NWs is stress-gradient-induced migration of point defects. Since the NW is held in an

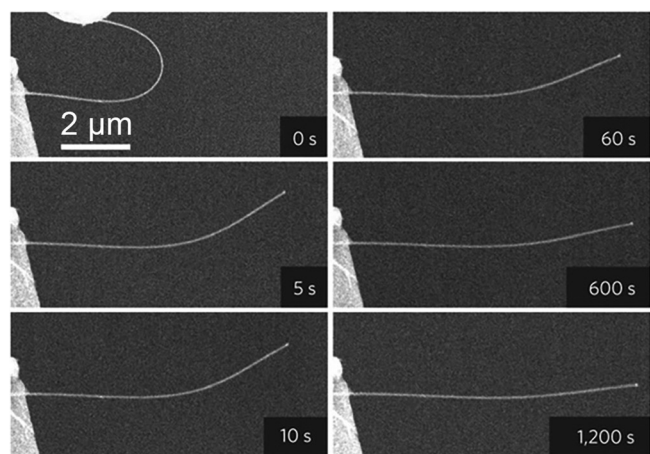


FIG. 16. A sequence of SEM images showing the recovery process for a ZnO NW after removing the bending load.<sup>170</sup> Reprinted with permission from Cheng *et al.*, Nat. Nanotechnol. **10**, 687 (2015). Copyright 2005 Nature Publishing Group.

ultra-large bent configuration for a certain time, a stress gradient formed across the NW, along which point defects migrate. Electron energy loss spectroscopy (EELS) measurements substantiated that the difference of oxygen concentration is almost linearly related to the anelastic strain, with the tensile side always richer in oxygen than the compressive side, suggesting that during recovery, oxygen vacancies could diffuse from the tensile to the compressive side, while zinc interstitials diffuse in the opposite direction.

#### E. Strength

Inspired by the classical work of Frenkel,<sup>173</sup> the theoretical strength of a material was estimated to be within the range of  $\mu/30$ – $\mu/15$ , in which  $\mu$  is the elastic shear modulus.<sup>174</sup> However, the actual strength of most materials is orders of magnitude lower than the theoretical one.<sup>175</sup> To rationalize this huge discrepancy, fracture mechanics and dislocation theory were developed for brittle and ductile materials, respectively.<sup>125</sup> Based on the two theories, the ideal strength could only be expected in perfect crystals, while real materials containing pre-existing imperfections, including micro-cracks and dislocations that determine the mechanical response of materials, have much lower strength. When the dimensions of materials are reduced to the nanometre regime, the possibility for the materials with few or even no internal defects increases significantly, which enables the materials' ability to sustain high stress before failure. Early studies showed that the yield strengths of Fe and Cu whiskers with diameters down to a few micrometres are over ten times higher than that of their bulk counterparts.<sup>31</sup> This phenomenon was caused by a decreased defect (dislocations) density with reduced sample dimensions.<sup>176</sup> During the last decade, uniaxial compression tests of single crystalline metallic pillars fabricated by FIB have shown that the yield strength of the pillars increases dramatically as their diameters decrease from 10  $\mu\text{m}$  to 100 nm, which is known as “smaller is stronger.”<sup>34,177</sup>

A substantial size effect on the yield strength of Au can be seen when the yield strength of pure Au from a number of

different studies and this is summarized and plotted as a function of lateral specimen dimension (Fig. 17).<sup>178</sup> As early as 1993, the deformation properties of Au NWs with diameters less than 20 nm were investigated using an AFM/STM-tip-based technique for probing.<sup>179</sup> The technique takes advantage of the high adherence ability of Au to obtain Au NWs with diameters of several nanometres by dipping the STM probe tips into Au and pulling atomic wire from the contact. The yield strength of Au NWs with diameters ranging from 4 to 8 nm attains a rather constant value of about 4 GPa,<sup>179</sup> which is substantially higher than that of bulk (55 to 200 MPa),<sup>180</sup> and close to the ideal strength of 5.5 GPa.<sup>181,182</sup> AFM bending of Au NWs showed similar values of yield strength, with average values of 5.6 GPa and 3.5 GPa for NWs with a diameter of 40 nm and 200 nm, respectively.<sup>29</sup> *In-situ* quantitative tensile tests on individual ⟨111⟩ single crystalline ultra-small Au NWs with uniform diameters ranging from 7 to 10 nm showed a yield strength of 1.1 GPa and a true fracture strength of 7 GPa.<sup>183</sup> The increased strength of Au NWs is a result of the reduction in the number of defects in the NWs. When the NWs diameter is further reduced from nanometres to the atomic scale, another increase in strength was provoked.<sup>178</sup> At the atomic scale, surface dislocations of NWs cease to nucleate, atomic chains deformed via ideal tensile atomic separation (quantized plasticity) with the measured yield strength of typically around or even above the theoretical predictions.<sup>183,184</sup>

Obvious size-dependence of yield strength was also revealed in other metallic NWs. The yield strength of Ag NWs contains fivefold twins increasing from 0.71 to 2.64 GPa as the diameter decreases from 130 to 34 nm.<sup>114</sup> The size effect in yield strength is attributed to the stiffening size effect in Young's modulus. *In-situ* tensile tests of single-crystalline Cu NWs with diameters from 75 nm to 300 nm were performed in SEM.<sup>185</sup> Due to the absence of dislocations, apparent brittle fracture occurred at stresses in the range of 1 GPa to 7 GPa, which is over 1000 times larger than the yield strength of high purity bulk single crystalline

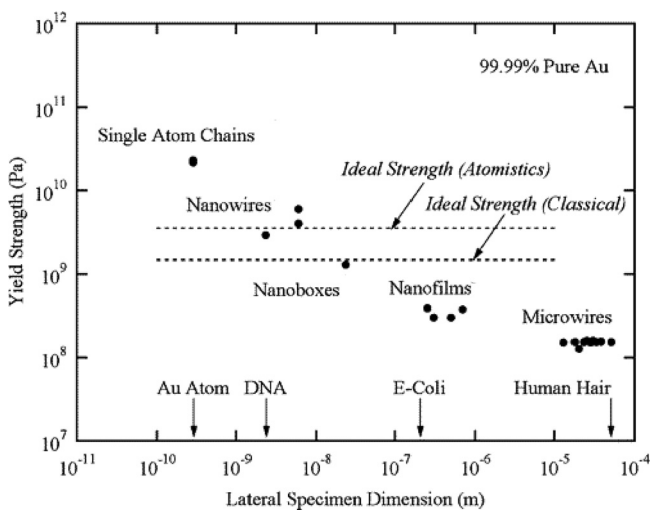


FIG. 17. Ideal predictions and experimental measurements regarding the yield strength of 99.99% pure Au as a function of lateral specimen dimension.<sup>178</sup> Reprinted with permission from Gall *et al.*, Nano Lett. **4**, 2431 (2004). Copyright 2004 American Chemical Society.

Cu and also higher than the measured yield strengths of microscale Cu whiskers.<sup>31,186</sup> The strength of NWs with diameter of 75 nm is close to the theoretical values.<sup>185</sup> The NWs are single crystals with few defects, while the deformation is expected to occur through slip of dislocations nucleated from free surfaces. Slip localized to one single crystalline plane due to the absence of defects in the vicinity that can trigger subsequent plastic deformation, resulting in brittle fracture and ultrahigh strength of the Cu NWs.

The yield strength of defect-free single crystalline Pd NWs increases from ~1 GPa to ~4 GPa as the NW diameter decreases from 260 nm down to 40 nm [Fig. 18(a)].<sup>187</sup> The plastic deformation of Pd NWs is mediated by the nucleation and slip of partial dislocations from the free surface. The stress required for the nucleation of the partial dislocations from the surface increases with the decrease in the NW diameter, leading to the size dependence of the yield stress. However, recent investigation of defect-scarce Pd NWs shows that there is apparent stochasticity of the measured strength of dislocation nucleation spanning several GPa due to a probabilistic thermally activated deformation process, indicating weak size effects of dislocation nucleation stress

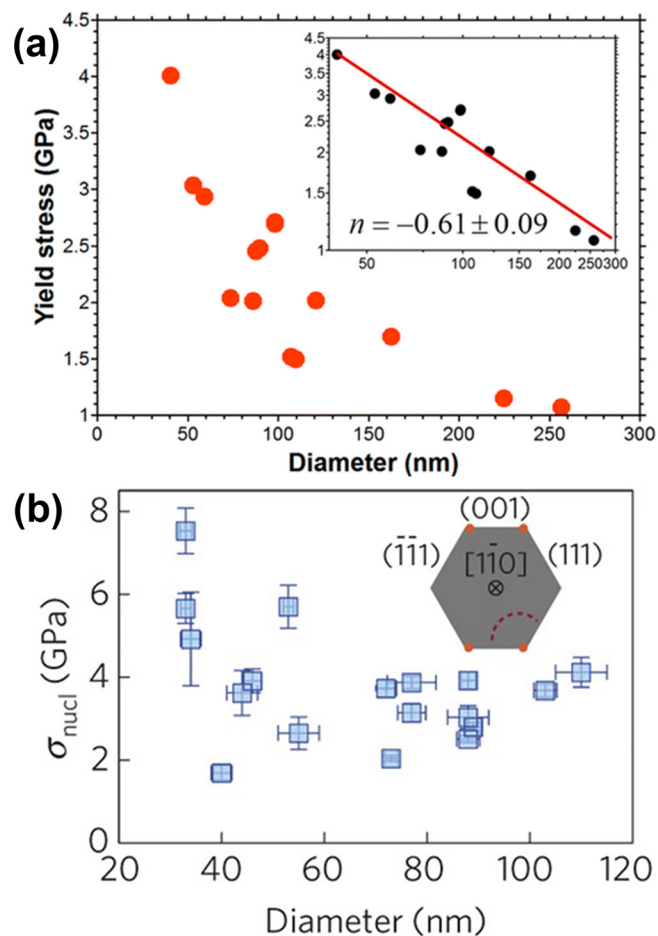


FIG. 18. (a) Size-dependence of the yield stress for the ⟨110⟩/⟨111⟩ Pd NWs.<sup>187</sup> Reprinted with permission from Seo *et al.*, Nano Lett. **13**, 5112 (2013). Copyright 2013 American Chemical Society. (b) Nucleation strengths measured in Pd NWs across a range of diameters at  $T = 295$  K and strain rates of the order of  $10^{-4}$  s<sup>-1</sup>.<sup>188</sup> Reprinted with permission from Chen *et al.*, Nat. Mater. **14**, 707 (2015). Copyright 2015 Nature Publishing Group.

in defect-free NWs [Fig. 18(b)].<sup>188</sup> This discrepancy may be attributed to the shapes of NWs, whose cross-sections are rhombic and hexagonal, respectively, since viable sites for dislocation nucleation are generally at edge corners. More experimental and theoretical investigations are needed to clarify whether the size effects on the nucleation stress of dislocations exist and if they depend on the geometry of NWs.

Apart from the diameter of metallic NWs, loading condition has also a significant effect on their yield strength.<sup>39</sup> AFM investigations indicated that the magnitude of the tensile yield strength of Au NWs is much larger than that of their compressive yield strength, which is so-called yield strength asymmetry.<sup>189</sup> MD simulations provided a mechanistic explanation for this asymmetry, which is due to the effects of surface stresses and different active slip systems during tensile and compressive deformation.<sup>190,191</sup> Due to the experimental difficulty, it is still challenging to experimentally testify the yield strength asymmetry.

Similar to metallic NWs, the strength of ceramic NWs is much higher than that of their bulk counterparts. AFM-based bending tests showed that the measured maximum fracture strength of SiC NWs was 53.4 GPa,<sup>78</sup> which is much larger than the corresponding values for bulk SiC and microscale SiC whiskers. The fracture strengths of various ceramic NWs have also been extensively investigated. Generally, the fracture strength of NWs increases with the decrease in the diameter, exhibiting the size effect. The fracture strength of Si NWs increased from 5.1 to 12.2 GPa, as the NW diameter decreased from 60 to 15 nm.<sup>50</sup> Such a size effect on fracture strength was related to the reduced numbers of surface defects in NWs with small diameters. In fact, Weibull statistics revealed that fracture strength of ceramic NWs could be significantly affected by surface area.<sup>73,114</sup> Therefore, the strength of Si NWs increases with the decrease in their side surface area.<sup>29–31</sup> Similar size effects in fracture strength have also been reported for other ceramic NWs.<sup>53,57</sup> Using a microelectromechanical systems (MEMS) testing stage, the tensile fracture strength of GaN NWs was measured to be in the range of 4 to 7 GPa.<sup>52</sup> Ultrahigh strength of 3.7 to 10.3 GPa was also reported in the ZnO NWs by uniaxial tensile testing.<sup>52</sup> However, no clear size effect was discovered for the bending fracture strength of Si and ZnO NWs.<sup>36–38,40,48</sup> For example, the bending fracture strength of Si NWs with diameters of 90 to 140 nm was found to be in the range of 7 to 18 GPa without showing a clear size effect.<sup>40</sup> Since the fracture of ceramic NWs could be ascribed to the surface defects, a strong size effects should be expected. However, the fabrication of NWs may significantly affect the density of surface defects and then surface quality should be considered for the comparison of the fracture strength of NWs. In addition to the diminished number of surface defects in small NWs, surface strengthening caused by the bond-length contraction of surface atoms also contributes to the size effect of the fracture strength.<sup>51</sup> Structural reconstruction on materials surface leads to reduced bond length and this strengthens the materials on the surface. Reducing the dimensions of NWs increases the surface-to-volume ratio of the NWs and therefore leads to higher fracture strength. Quantifying the

detailed roles of each factor will be necessary for comprehensive understanding of the fracture behavior of NWs.

## F. Plasticity

Deformation mediated by mechanisms including dislocation slip and deformation twinning is usually permanent or irreversible and is called plastic deformation. Since the small size scale of NWs makes dislocation activities very difficult due to the geometrical constraints and limits the number of defect sources inside NWs, the plasticity of NWs varies remarkably from that of their bulk counterparts. The plasticity of metal NWs predicted by atomistic simulations has been comprehensively reviewed,<sup>38,39</sup> the results from MD simulations show that plasticity in metal NWs with diameters below 100 nm is dominated by the dislocation nucleation from free surfaces, and perfect or partial dislocation slip and deformation twinning. Therefore, this review paper mainly focuses on the plastic deformation mechanisms of metallic and ceramic NWs observed by experimental investigations and also includes a brief comparison between experimental results and theoretical predictions.

Generally, metallic NWs with diameters less than 100 nm are expected to be free of dislocations before loading.<sup>177</sup> This implies that at the onset of yielding, no mobile dislocation is available in the NWs to accommodate plastic strain. In lieu of conventional dislocation multiplication, storage, and interaction, dislocation nucleation from the surface of NWs becomes increasingly significant for their deformation behaviour. In defect-free NWs, a leading partial dislocation will be firstly nucleated on the NW free surface during plastic deformation. There are three possible scenarios in the deformation process: (1) if the leading partial is immediately followed by a trailing partial on the same slip plane, this leads to slip by a full dislocation; (2) if the trailing partial is nucleated on the same plane but keeping a substantial distance from the leading partial, or if there is no subsequent trailing partial, slip by partial dislocations will result in the formation of SFs; and (3) if another leading partial is nucleated on a parallel slip plane adjacent to the first slip plane, deformation twinning occurs. It is apparent that deformation twins and SFs are the footprints of partial dislocation activities.<sup>39,192,193</sup> In fact, full dislocation slip, partial dislocation slip, and deformation twinning have been observed in metallic NWs and these mechanisms are in direct competition. Apart from the intrinsic material parameters (such as SF energy), the deformation mechanisms of NWs are also influenced by many other factors, including the crystallographic orientation and diameter of NWs, surface structure, and the loading condition. Detailed information of theoretical analysis about these factors can be referred to the review articles presented in Refs. 38 and 39.

The effect of crystallographic orientation of NWs and loading conditions on the choice of deformation mechanism can be largely explained by the Schmid factor, which describes the resolved shear stress on a given slip system. According to the Schmid law, the most active slip system is the one with the highest Schmid factor.<sup>174</sup> Schmid factors for partial and perfect dislocations on the most active {111} slip

plane in FCC metallic NWs under different loading conditions are summarized in Table II.<sup>39</sup> If the Schmid factor of the trailing partial is larger than that of the leading partial, slip by full dislocations will dominate the deformation, e.g.,  $\langle 100 \rangle$  and  $\langle 111 \rangle$  NWs in tension and  $\langle 110 \rangle$  NWs in compression. If the Schmid factor of the trailing partial is smaller than that of the leading partial, SFs or deformation twins will be expected, e.g.,  $\langle 110 \rangle$  NWs in tension and  $\langle 100 \rangle$  and  $\langle 111 \rangle$  NWs in compression. Although Schmid factor is purely a geometric factor, crystallographic orientation- and loading direction-dependent deformation mechanisms of NWs have been largely confirmed by experimental observations. For example, plastic deformation of  $\langle 110 \rangle$  Au NWs with a diameter of  $\sim 140$  nm under uniaxial compression was mediated by full dislocation slip, leaving the slip steps on the NW surface. However, deformation twinning played a dominant role in the plastic deformation of  $\langle 110 \rangle$  Au NWs deformed by tension.<sup>194,195</sup> Moreover, deformation twining in these NWs with diameters of 40–150 nm and lengths of 5–20  $\mu\text{m}$  enables them to have superplastic deformation and reorient the crystal from  $\langle 110 \rangle$  to  $\langle 100 \rangle$  during tensile deformation. The importance of Schmid factor in determining the deformation mechanisms is also evidenced by the deformation of in BCC W NWs with diameters of 10–20 nm that have similar critical resolved shear stresses for deformation twinning and slip.<sup>179</sup> Deformation twinning is the predominant deformation mode of BCC W NWs when loaded along  $\langle 100 \rangle$ ,  $\langle 110 \rangle$ , and  $\langle 111 \rangle$  directions since the Schmid factors of twinning systems are larger than those of slip systems, while dislocation mediated plasticity is the primary mechanism for  $\langle 112 \rangle$  loading due to the larger Schmid factor of slip than that of twinning.<sup>196</sup> As a whole, Schmid factor plays an essential role in affecting the plasticity of NWs and can be applied to predict the activation of deformation mechanisms.

Decreasing the size of metallic structures not only changes the mechanical properties (such as Young's modulus and strength)<sup>29,83,131,197</sup> but also alters the deformation mechanism.<sup>37,198</sup> For FCC metals, a transition from full dislocation slip to partial dislocation activity has been reported when their characteristic size (for example, grain size of nanocrystalline Al<sup>199</sup> and film thickness of single crystalline Au films<sup>200</sup>) decreases to several tens of nanometres. The effect of NW diameter on deformation mechanism was quantitatively revealed by *in-situ* HRTEM tensile tests of Cu NWs with diameters ranging from 70 to 1000 nm.<sup>116</sup> It was found that NWs with large diameters deformed predominantly by full dislocation slip. When the diameter of the NW is reduced to below  $\sim 200$  nm, partial dislocation slip (SFs and deformation twins) gradually becomes the dominant mechanism. When the diameter was reduced to  $\sim 134$  nm, partial dislocation activities almost entirely replaced the full-slip. Quantitative assessment of relative contributions of each deformation mechanisms showed a clear crossover for plasticity carrier from full dislocations to partial dislocations when the diameter of the NWs decreases to the  $\sim 100$  nm range, indicating a sample size effect on the deformation mechanisms of NWs.

Since dislocations mainly nucleate from the surface of NWs, surface structure also affects significantly deformation

mechanisms. For defect-free  $\langle 110 \rangle$  Pd NWs with a hexagonal cross-section bounded by four  $\{111\}$  and two  $\{001\}$  side facets, slip by identical partials from free surface was observed during tensile deformation.<sup>188</sup> However, deformation twining, which induce crystallographic reorientation, plays a dominant role in the superplastic deformation in defect-free  $\langle 110 \rangle$  Pd NWs with a rhombic cross-section bounded by four  $\{111\}$  side facets.<sup>187</sup> The different deformation mechanisms in these two types of Pd NWs were attributed to the type of surface crystallographic planes that determine the surface energy. In addition, surface roughness also influences the choice of deformation mechanisms. Recent *in-situ* HRTEM observations of tensile deformation of sub-10-nm Au NWs manifested that full dislocation slip and deformation twinning are favoured for  $\langle 001 \rangle$  and  $\langle 110 \rangle$  NWs, which complied to the prediction based on their Schmid factors.<sup>201</sup> However, deformation mechanism of Au NWs can change from dislocation slip to twinning under the same  $\langle 001 \rangle$  loading direction due to the abundance of  $\{111\}$  terraces on the surface, facilitating the nucleation of twinning partials. Another *in-situ* HRTEM experiments revealed that full dislocations are prevalent in ultrathin Ag NWs with diameters of 5 and 11 nm.<sup>122</sup> This result also contradicts the prediction from MD simulations,<sup>202,203</sup> which could be attributed to the surface energy and morphology.

Plastic deformation mediated by partial dislocation activities was also observed in sub-20-nm-sized  $\langle 111 \rangle$  Au NWs, leading to ductile fracture in tension.<sup>104</sup> However, brittle-like fracture was observed when there was a misalignment of  $\sim 25^\circ$  between the tensile loading direction and the NW axis. This unexpected brittle fracture is a result of shear-induced twinning and the initiation of the fracture near the intersection of the initial twin boundary (TB) with the NW surface. These results emphasize the importance of loading condition in determining the dominant deformation mechanism and fracture mode.

Different from metallic materials, activation of dislocation activities in ceramic materials requires high stress because of their ionic/covalent bonding nature.<sup>125</sup> Due to the existence of flaws in bulk ceramic materials, ceramics usually fracture at a stress lower than the critical resolved shear stress required to initiate dislocation-mediated plastic deformation.<sup>125</sup> As such, bulk ceramic materials are brittle in nature and tend to fracture catastrophically in a brittle manner after only a small elastic strain of  $\sim 0.1\%$  without dislocation-mediated plasticity.<sup>125</sup>

TABLE II. Schmid factors for partial and perfect dislocations in FCC metallic NWs under different loading conditions.<sup>39</sup>

Orientation	Loading	Leading partial	Trailing partial	Perfect dislocation
$\langle 100 \rangle$	Tension	0.24	0.47	0.41
$\langle 100 \rangle$	Compression	0.47	0.24	0.41
$\langle 110 \rangle$	Tension	0.47	0.24	0.41
$\langle 110 \rangle$	Compression	0.24	0.47	0.41
$\langle 111 \rangle$	Tension	0.31	0.16	0.27
$\langle 111 \rangle$	Compression	0.16	0.31	0.27

When the dimensions of ceramic materials reduce to a small scale, defect-free structures can be obtained, which makes it possible for the materials to sustain high stress and high strain before fracture. This stress could be high enough to overcome the critical resolved shear stress and supply sufficient energy to nucleate and/or move glissile dislocations. In addition to the defect-free structures, the high surface-to-volume ratios in NWs could also be responsible for the development of plasticity because the surface of the NWs provides abundant dislocation-nucleation sites, and much lower stress is needed for dislocation nucleation at the surface than dislocation self-multiplication within crystals.<sup>193,204</sup> The earliest atomic scale observations of unusual large-strain plasticity of ceramic (Si and SiC in these cases) NWs at room temperature were reported in 2007.<sup>43,44</sup> This opened a new research field of atomic scale *in-situ* investigation of the deformation mechanisms of nanomaterials. Further, with electron beam illumination, superplasticity of SiC NWs with >200% elongation<sup>46</sup> was achieved by *in-situ* axial-tensile experiments in SEM, indicating the possibility of using an electron-beam-assisted technique, other than the techniques of lithography, to fabricate nano-sized objects including NWs. Later, it has been demonstrated that Ge NWs tolerate diameter-dependent flexural strain of up to 17% before fracture, and their crystalline structure transforms to an amorphous structure at the maximum strain.<sup>143</sup> The detailed mechanism of the mechanically induced amorphization process could be similar to that of SiC NWs under bending<sup>44,85</sup> and TiNi deformed by high-pressure torsion,<sup>205</sup> but further study is required. Similarly, ZnO NWs also experienced a crystal-to-amorphous transition in highly compressed regions after a number of loading and unloading cycles.<sup>133</sup> A summary of the fracture modes and failure strain, including the values of plastic strain in some cases, is listed in Table I.

*In-situ* HRTEM investigations revealed that large plastic strain of Si NWs during bending deformation is caused by the nucleation and interactions of mobile full dislocations, which could lead to the formation of Lomer lock dislocations, and structural disordering.<sup>55</sup> A typical example of the formation of a Lomer lock via two full dislocations is presented in Fig. 19, in which the two dislocations had Burgers vectors of  $b = \frac{1}{2}[011]$  [Fig. 19(a)] and  $b = \frac{1}{2}[10\bar{1}]$  [Fig. 19(b)], respectively, and the resulting Lomer lock dislocation had a Burgers vector of  $\frac{1}{2}[110]$  that is perpendicular to the slip plane [Fig. 19(c)]. An enlarged HRTEM image of the Lomer lock structure is presented in Fig. 19(d). Continuously increasing the bending strain results in atomic disorder at the core of a Lomer lock that eventually transforms the local area into an amorphous structure, as revealed in two HRTEM images taken from the same region at different strain values [Figs. 19(e) and 19(f)]. These results clearly demonstrated that ultra-large plasticity in some ceramic NWs is caused by extensive dislocation activities and a crystal-to-amorphous phase transition. A recent *in-situ* bending HRTEM investigation of Si NWs<sup>206</sup> showed that the deformation mechanism of Si NWs is affected by the sign (tensile or compressive) and magnitude of the applied stress. It was found that the deformation mechanism of bent Si NWs transformed from the full-dislocation-dominated plasticity in the early stages of deformation to significant partial dislocation activities when the bending strain was >6.7%. Apart

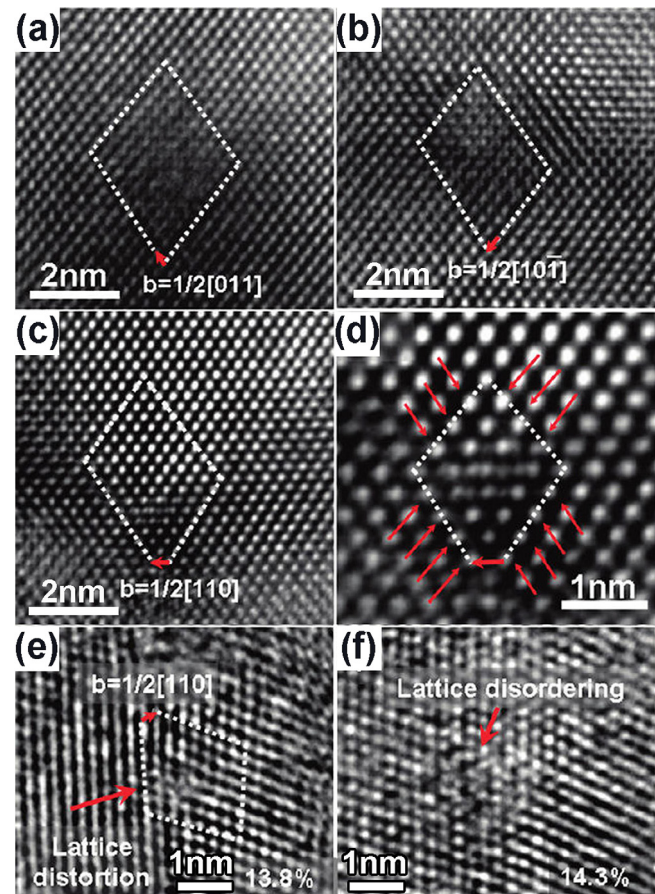


FIG. 19. An atomic-scale *in-situ* observation of a Lomer lock dislocation-formation process via a dislocation reaction and the subsequent crystalline to amorphous transition. (a) and (b) A glissile dislocation with a Burgers vector of  $b = \frac{1}{2}[011]$  and  $\frac{1}{2}[10\bar{1}]$ , respectively. (c) A Lomer lock dislocation formed via the reaction of the two dislocations shown in (a) and (b). (d) An enlarged HRTEM image showing the Lomer lock structure. (e) and (f) Enlarged HRTEM images showing a crystalline to amorphous transition process at the atomic scale.<sup>55</sup> Reprinted with permission from Wang *et al.*, Nano Lett. **11**, 2382 (2011). Copyright 2011 American Chemical Society.

from the strain/stress magnitude, the sign of the stress has an obvious effect on the dislocation type. Partial dislocations were always generated from the tensile stressed region, while only full dislocations were observed in the compressively stressed region.<sup>206</sup> This phenomenon was neglected in most of the previous experimental observations.<sup>44,55,85</sup> These unprecedented findings are extremely valuable not only in scientific research for understanding the atomic scale deformation mechanism of ceramic NWs but also in the technological way for development of novel Si NW-based devices.

Controversial results have been reported for the deformation behavior of ceramic NWs. Several studies have demonstrated that ceramic NWs are brittle without any noticeable plastic deformation before catastrophic fracture under both uniaxial tension and bending. For example, both bending tests<sup>40,48,207</sup> and tensile deformation<sup>50,53,57,208</sup> of Si NWs demonstrated only brittle fracture, which was evidenced by cleavage fracture along the {111} planes without any obvious necking or sliding and a linear elastic deformation before an abrupt drop in the stress caused by failure. ZnO NWs have also been found to deform elastically until brittle fracture under bending.<sup>42,45,47</sup>

These discrepancies indicate that the mechanical behaviors of ceramic NWs are complicated and depend on many factors, including strain rate, loading condition, sample size, sample orientation, and sample defects, as discussed in the following paragraphs.

- (1) Strain rate effects: It is well known that the mechanical behaviors of materials (e.g., brittle-to-ductile [BTD] transition) are sensitive to strain rate.<sup>209,210</sup> The critical BTD transition temperature increases with the increase in the strain rate. Large plastic strain is usually obtained at low strain rates, for example, Si NWs under bending or tension with a strain rate of approximately  $10^{-5} \text{ s}^{-1}$ <sup>43,44</sup> and Ge NWs under bending with a strain rate of  $10^{-3} \text{ s}^{-1}$ .<sup>143</sup> High strain rates might result in brittle fracture. However, Si NWs have demonstrated brittle fracture when bent at a speed of 10–30 nm for a distance of 100–300 nm.<sup>48</sup>
- (2) Stress state effects: Under different loading conditions, the stress state varies remarkably and therefore affects plastic deformation in various ways. A stress-state parameter ( $\alpha$ ) of the ratio between the maximum shear stress and the maximum axial-tensile stress can be defined to describe the influence of the stress state on the ductility of a material:  $\alpha = (\tau_{max})/(S_{max}) = (\sigma_1 - \sigma_3)/(2[\sigma_1 - \nu(\sigma_2 + \sigma_3)])$ , where  $\tau_{max}$ ,  $S_{max}$ ,  $\sigma_{1,2,3}$ , and  $\nu$  are the maximum shear stress, maximum tensile stress, three principal stresses, and Poisson's ratio, respectively.<sup>175</sup> The  $\alpha$  value for uniaxial tension and compression is  $\sim 0.5$  and  $\sim 2$ , respectively. Materials tend to be more brittle with a smaller  $\alpha$  value. The stress state under bending is complex, with one side being under tension and the other side being under compression. Si NWs fractured in a brittle manner under tension but deformed with pronounced plastic deformation under compression and bending.<sup>57</sup>
- (3) Size effects: It has been proposed that the plasticity of a particular material is controlled by the dislocation velocity, which is regarded as the rate of emission of dislocations and/or dislocation motion.<sup>43</sup> The dislocation velocity is diameter dependent.<sup>211</sup> NWs with a small diameter have a high dislocation velocity and tend to be ductile. For example, while GaAs NWs are usually brittle, obvious plastic deformation through dislocation activities occurs in GaAs NWs with diameter smaller than 25 nm.<sup>54</sup> Under a bending condition, brittle fracture was observed for Si NWs with diameters in the range of 100–700 nm<sup>48</sup> and ductile deformation presented in Si NWs with diameters between 15 and 70 nm.<sup>43</sup>
- (4) Effects of orientation and defects: The effect of crystallographic orientation relative to the loading direction can be described by “ductility parameter”:<sup>59</sup>  $A \equiv (S\sigma_c)/\tau_c$ , where  $S$  is the Schmid factor for the most active slip system,  $\sigma_c$  is the ideal tensile strength, and  $\tau_c$  is the ideal shear strength. The “ductility parameter” accounts for the combined effect of  $(S\sigma_c)$  and  $\tau_c$ . Slip induced plasticity occurs on a slip system when the resolved shear stress  $\tau_{RSS}$  on the slip system reaches a critical value  $\tau_c$ . The resolved shear stress  $\tau_{RSS}$  can be related to the applied uniaxial stress  $\sigma$  through the relation  $\tau_{RSS} = S\sigma$ . A large  $A$  value ( $A > 1$ ) indicates that  $S\sigma_c$  is larger than  $\tau_c$ , i.e., the material is stronger in tension

than in shear, and will exhibit slip induced ductile fracture. Conversely, a small  $A$  value ( $A < 1$ ) indicates that the material will fail by brittle fracture. Ductile or brittle fracture can be predicted based on whether  $A$  is greater or less than 1.<sup>59</sup> It has been found that Si NWs with  $\langle 111 \rangle$  growth directions have a smaller  $A$  value and are more brittle than those with  $\langle 110 \rangle$  growth directions.<sup>59,62</sup> Defects, such as surface steps or TBs, may act as stress concentrators and initiation sites for cracks, facilitating a brittle fracture,<sup>48,57</sup> while ductility may be observed in a defect-free NW.<sup>43</sup> In addition, experimental conditions, such as electron-beam irradiation,<sup>212</sup> NW clamping, and loading alignments,<sup>130</sup> could also affect the mechanical behaviors of NWs.

Plastic deformation is non-recoverable or permanent in bulk materials. However, reversible plasticity has been observed in GaAs NWs during bending deformation processes.<sup>87</sup> As presented in Fig. 20(a), a high density of dislocations was found across a bent GaAs NW. After the release of the bending stress, the dislocation density in the recovered NWs reduced dramatically [Fig. 20(b)]. It is known that NW has very high surface-to-volume ratio, and the surface of NWs provides abundant sources for dislocation nucleation and acts as the sink for dislocation annihilation. Hence, during the bending deformation of a NW, a very high density of dislocations nucleates from the surface of the NW. For bending deformation of a NW, the stress status changes from tension at one side of the NW to compression at the other side. There is a transition zone somewhere around the geometric axial center of the NW with zero stress. Such a zero-stress area acts as a barrier to prevent dislocations from passing through the whole NW. Consequently, the tangling of dislocations results in significant strain hardening, leading to a very rapid increase in the flow stress and further increase in significant elastic strain after the initiation of plastic deformation. When the load is removed, the recovery of elastic strain produces large internal stress, which is opposite in direction and approximately equivalent in magnitude to the applied stress. This internal stress spontaneously drives the dislocation motion backwards and finally, most of the dislocations annihilate at the NW surface from which they nucleate. Therefore, the plastic strain is recovered through the reverse motion of the dislocations. The time-dependent and fully reversible plasticity also exhibits in the fivefold twinned Ag NWs,<sup>112</sup> which is discussed in Sec. IV.

## G. Fatigue

With respect to the perspective applications of NWs as critical components in nanodevices, apart from their static mechanical properties, their fatigue resistance, i.e., their resistance to failure when subjected to cyclic deformation, is also crucial since fatigue is a commonly encountered failure mode that determines the stability, integrity, and lifetime of NW-based devices.<sup>95</sup> However, performing a fatigue experiment on a NW is very difficult due to the small size of the NW and the fact that fatigue test is an extremely time-consuming experiment, which usually requires  $\sim 10^8$  loading cycles.<sup>125</sup> As a result, investigations of cyclic deformation responses of NWs have been very limited.

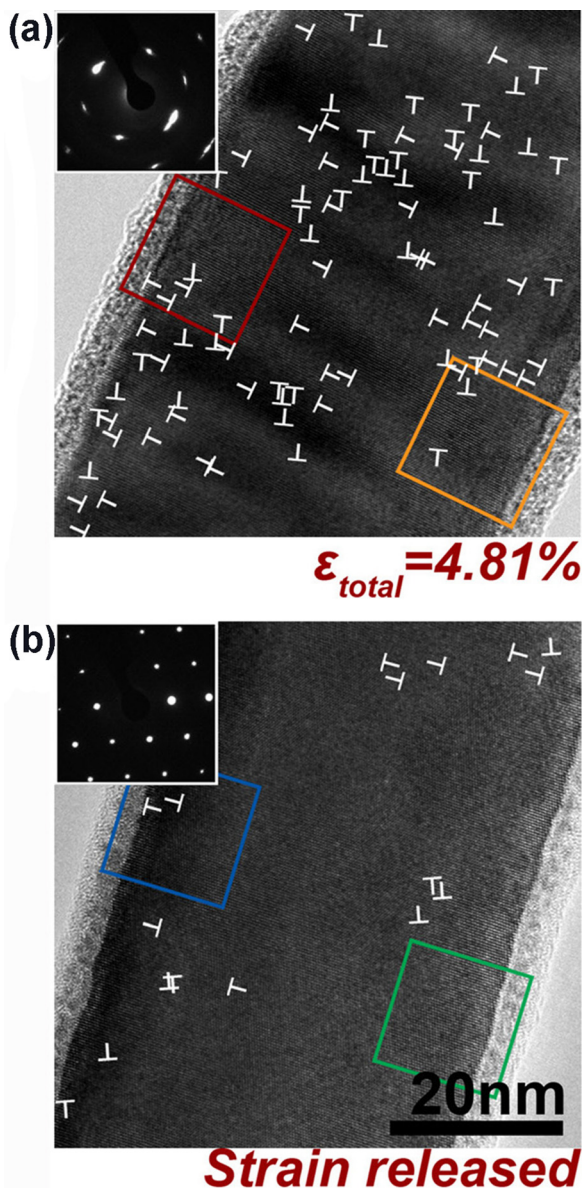


FIG. 20. The microstructural evolution of a GaAs NW during a bending–release process. (a) An HRTEM image and corresponding SAED pattern of a NW deformed 4.81%. A very high density of dislocations is seen. (b) An HRTEM image of the NW following removal of the applied load. The inset SAED pattern is identical to that of the undeformed sample.<sup>87</sup> Reprinted with permission from Appl. Phys. Lett. **104**, 021904 (2014). Copyright 2014 AIP Publishing LLC.

So far, only the fatigue behaviors of ZnO NWs have been studied using the resonance method.<sup>94,95</sup> *In-situ* TEM fatigue studies revealed that intact ZnO NWs are free of fatigue after high-cycle loading up to  $10^{10}$  cycles.<sup>94,95</sup> Defects in materials act as local stress concentrators, just like the unavoidable defects (e.g., dislocations and cracks) in materials always serve as sources for the nucleation and propagation of fatigue cracks. Therefore, the infinite fatigue life of intact NWs is caused by the defect-free nature of the NWs, which makes the crack nucleation extremely difficult. The large surface-to-volume ratio of NWs also contributes to the fatigue-free nature of ZnO NWs because the surface enhances the atomic mobility that allows the NWs to undergo cyclic deformation without fracture. However, a

ZnO NW that was irradiated by an electron beam before resonance testing fractured after resonance for seconds.<sup>95</sup> It has been proposed that the Joule heat of electron beam irradiation causes melting and local stress concentration.<sup>213</sup> Instead of uniform stress distribution in the intact NWs, local stress concentration promotes the fracture of electron-beam irradiated NWs. Timely advancing the knowledge of the fatigue behavior of NWs is important both scientifically, for the comprehensive understanding of their unique fatigue behavior, and technologically, for assessing their durability as a safety-critical structural components, and for guiding the design, fabrication, and optimization of NW-based devices.

#### IV. EFFECTS OF PLANAR DEFECTS ON THE MECHANICAL BEHAVIOURS OF NWs

It is well established that planar defects including SFs and twins can significantly affect the mechanical properties and deformation mechanisms of materials.<sup>214–222</sup> When a high density of coherent nanoscale twins is introduced into materials, superior mechanical properties including high strength and ductility, excellent thermal stability and high electrical conductivity could be harvested simultaneously.<sup>223–226</sup> In fact, the nanoscience and nanotechnology community increasingly realizes that the concept of planar-defect engineering can also be applied to tune the mechanical, physical, and chemical properties of NWs.<sup>227,228</sup>

The interatomic bonding of materials may be altered at the defect areas and this might affect the Young's modulus. Depending on materials and the type and orientation of defects, the effect of planar defects on Young's modulus varies.<sup>229,230</sup> For example, introduction of profuse SFs leads to a higher Young's modulus than defect-free NWs.<sup>58,71</sup> As shown in Fig. 21, irrespective of the diameters of GaAs NWs with a hexagonal wurtzite structure, the presence of high densities of SFs increases the Young's modulus by  $\sim 13\%$ .<sup>163</sup> However, experiments<sup>107</sup> and simulations<sup>231</sup> demonstrated that crystalline defects in GaN NWs reduce the Young's modulus of the NWs. Another investigation revealed that the average value of measured Young's modulus of SiC NWs with highly defective structures in a periodic fashion is within the range for bulk SiC.<sup>232</sup> In contrast to ceramic NWs, experiments and simulations confirm that there is no apparent influence on the Young's modulus of metallic NWs when the introduced twins are perpendicular to the length direction or longitudinal axis of NWs.<sup>182,233</sup> Nevertheless, when a fivefold-twinned structure with five TBs parallel to the longitudinal axis of NWs is introduced, atomic simulations revealed that enhanced Young's modulus and size-dependent elasticity could be expected due to this intrinsically strained structures.<sup>234</sup> *In-situ* tensile testing of fivefold twinned Ag NWs presented a strong size effect in elasticity.<sup>113,114</sup> Further investigations and careful analysis are needed to understand the size effect. The intrinsic strain induced by fivefold twins seems to be significant only when the diameter of NWs is very small because the internal strain could be relaxed in fivefold-twinned NWs with large diameters.<sup>234</sup>

An atomistic study of NWs with uniform twin sizes suggested that the elastic strain limit is inversely proportional to

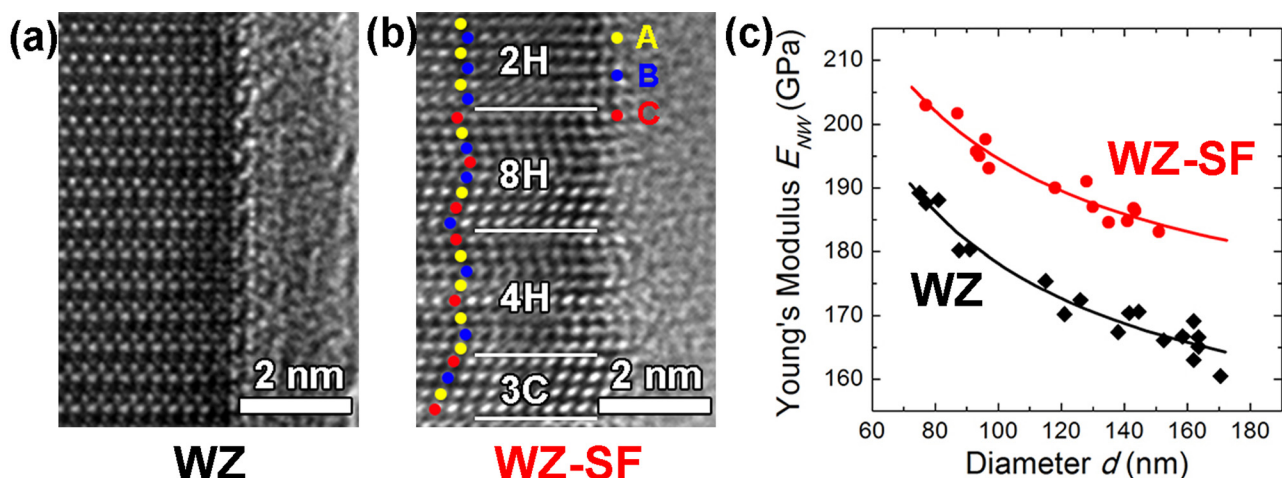


FIG. 21. HRTEM images of GaAs NWs without (a) and with SFs (b), and (c) the effects of SFs on the Young's modulus as a function of diameter.<sup>71</sup> Reprinted with permission from Chen *et al.*, Nano Lett. **16**(3), 1911–1916 (2016). Copyright 2016 American Chemical Society.

the twin thickness ( $\lambda$ ).<sup>235</sup> Recently, the dependence of elastic strain limit on twin thickness has been observed experimentally through *in-situ* HRTEM tensile tests<sup>106</sup> and atomic scale lattice strain measurements on Au NWs with TBs perpendicular to the NW axial direction.<sup>236</sup> Both the experimental and simulation results showed that there is a linear relationship between the elastic strain limit and  $\lambda^{-1/2}$  for twin thickness greater than  $\sim 3$  nm, which indicates a strong Hall–Petch type behaviour for elastic strain, as exhibited in Fig. 22. As the twin size decreases to below 3 nm, the elastic strain limit rises up to 5.3%, close to the ideal theoretical tensile elastic strain limit. The twin thickness dependence of the elastic strain limit is mainly attributed to the repulsive force on gliding dislocations exerted by TBs, which increases as twin thickness decreases.<sup>237</sup> Therefore, a higher stress is required for dislocation nucleation in NWs with TBs. As the twin size decreases below 2.8 nm, the deformation

mechanism by the heterogeneous nucleation from surface is no longer activated but the homogeneous nucleation, for which the stress required is close to the ideal shear stress of materials, independent of twin thickness.<sup>106</sup> Therefore, the elastic strain limit does not change much with twin thickness less than 2.8 nm and gradually converges to the ideal theoretical limit. These results are in agreement with another *in-situ* tensile test of Au NWs with different twin thicknesses.<sup>106</sup> This study also found that the elastic strain limit in NWs with non-uniform twin thickness is determined by the NW segment with the largest twin spacing, which supports the prediction of atomistic study.<sup>237</sup>

Since the 1920s, theoretical investigations endeavoured to explore the upper limit of lattice strain and predicated that the upper bound of lattice shear strain in metals can be over 30%.<sup>238,239</sup> Recently, a continuous and reversible lattice deformation with shear strain as high as 34.6% was observed experimentally in bending deformation of nanotwin-structured Ni NWs with NW growth direction nearly along a  $\langle 112 \rangle$  direction and irregular spaced twin lamellae parallel to  $\{111\}$  plane.<sup>67</sup> The observed strain of 34.6% is approximately four times as large as the ideal elastic strain limit in normal conditions. This extraordinary large strain is a result of the largely delayed plastic deformation since dislocation activities have been almost entirely suppressed by twin lamellae with thicknesses of 1 to 6 nm. The critical resolved shear stress required for dislocation nucleation increases as the twin thickness decreases. For NWs with twin thicknesses smaller than 6 nm, the required stress for the nucleation of full or partial dislocations is too high and even larger than the calculated maximum shear strength. As presented in Fig. 23, the lattice strain process of Ni NWs starts from the original face-centred cubic structure, transition through the orthogonal path to reach a body-centred tetragonal structure, and finally to a re-oriented face-centred cubic structure. This ultra-large shear strain is fully reversible during the unloading or after the onset of plastic deformation, which releases the large elastic energy stored in the NW to force all the sheared lattices back to the original face-centered cubic structure. The achievement of a super large lattice strain of

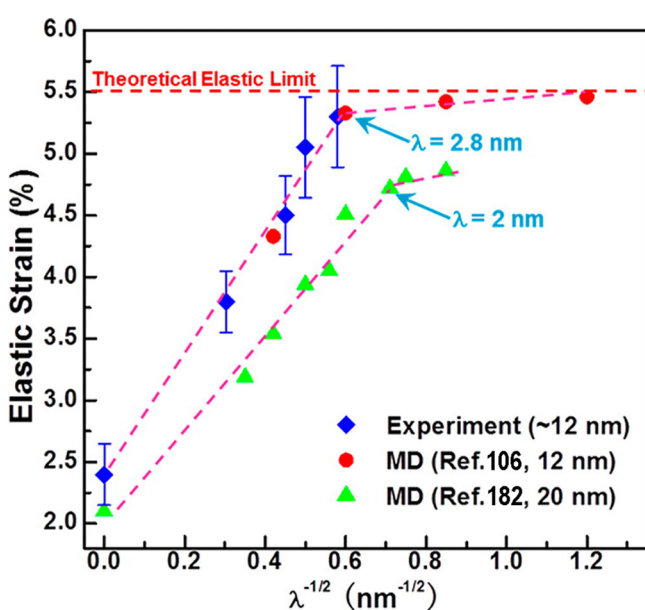


FIG. 22. Hall–Petch type behavior in the elastic strain limit of nanotwinned [111]-Au NWs.<sup>236</sup> Reprinted with permission from Wang *et al.*, Nano Lett. **15**, 3865 (2015). Copyright 2015 American Chemical Society.

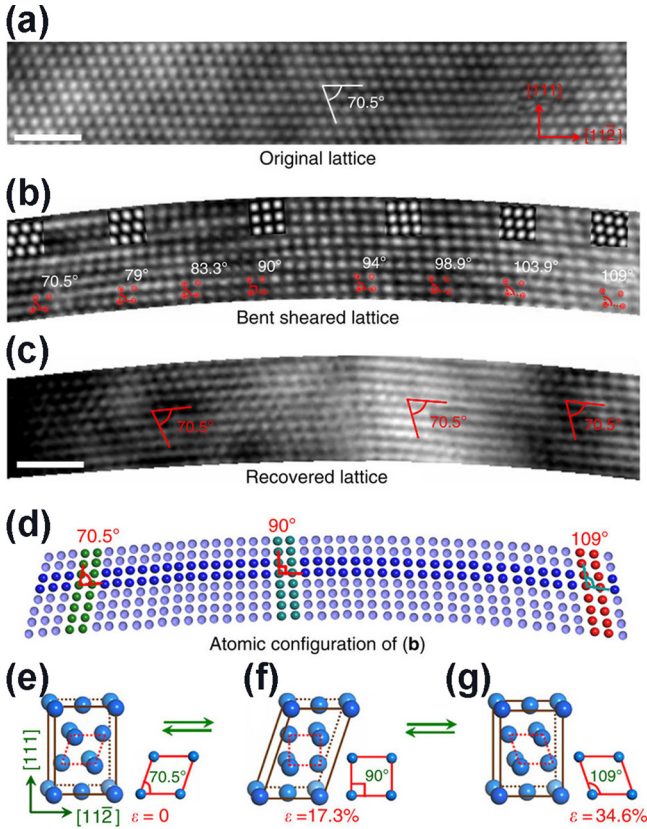


FIG. 23. (a) Atomic structures of a Ni NW subjected to the bent strain of  $\sim 1.9\%$ . (b) the continuous increase in inter-planar angle ( $\alpha$ ) of the  $\{111\}$  from  $71^\circ$  to  $\sim 109^\circ$ . The simulated HREM images are inserted accordingly. (c) HRTEM image after the strain released revealing the full recovery of  $34.6\%$  lattice shear strain. (d) Atomic configurations of the ultra-large continuous lattice shear from  $0$  to  $34.6\%$ . (e)–(g) Schematic illustration of the shear and recover process of the FCC lattice. The scale bars are  $1\text{ nm}$ .<sup>67</sup> Reprinted with permission from Wang *et al.*, Nat. Commun. **4**, 2413 (2013). Copyright 2013 Nature Publishing Group.

up to  $34.6\%$ , which is far beyond the theoretical lattice strain limit, is one of the most significant breakthroughs since the upper limit of lattice strain was predicated nearly 100 years ago.<sup>238,239</sup> This discovery demonstrates the significant capability of some nanomaterials in elastic strain energy storage and also presents the dramatic potential of elastic strain engineering for tuning the band gap of semiconductor nanomaterials.

Apart from the elasticity of NWs, planar defects also affect the anelastic behaviour of ceramic NWs. For example, compared with defect-free GaAs NWs, a relatively weak anelasticity was observed in GaAs NWs with a high density of SFs.<sup>105</sup> Anelastic strain of approximately  $0.5\text{--}1.0$  and  $0.3\text{--}0.6\%$  was recorded in NWs with a diameter of  $\sim 25\text{ nm}$  without and with stacking faults, respectively. The introduction of profuse SFs leads to a wavy amorphous/crystalline interfacial structure, which may affect the atomic bonding at the interfacial region and then reduce the relaxation behaviour. In addition, the planar defects (SFs) in the NW enable effective transfer of the residual stress from the amorphous layer to the crystal core, resulting in weak anelasticity in NWs with SFs. In contrast, large anelasticity, with elastic strain up to  $0.65\%$ , was reported for CuO NWs with a twinned structure.<sup>240</sup> The difference between the inelasticity reported in these two kinds of NWs can be ascribed to the

different operating mechanisms of recovery of the residual bending strain. Note that the anelasticity in GaAs NWs originates from the presence of the amorphous layer, which is not found in CuO NWs. The anelastic behaviour of CuO NWs was attributed to the motion of atoms in the vicinity of the TB. During the bending deformation, due to the low activation energy of atoms near grain boundaries, atoms adjacent to TBs would deviate from their original positions and move back to their initial positions by the global lattice distortion stress once the loading is released. To clarify the effect of electron beam irradiation on anelasticity, it was found that the residual strain could recover with turning off the electron beam, but at a lower recovery rate than the rate with electron beam irradiation.<sup>240</sup>

Although the strength of NWs has reached a significant fraction of the ideal strength of perfect crystals, there is still plenty of room to approach the ideal strength through microstructural design.<sup>182</sup> Recent studies revealed the remarkable strengthening effect of TBs on Au NWs. The average ultimate tensile strength of  $\langle 111 \rangle$  Au NWs with no twin, a low-density of twins, and an ultrahigh density of twins was  $1.43\text{ GPa}$ ,  $2.05\text{ GPa}$ , and  $3.12\text{ GPa}$ , respectively, as shown in Figs. 24(a) and 24(b).<sup>106</sup> The critical resolved shear stress of NWs with an ultrahigh density of twins for partial slip  $0.98\text{ GPa}$ , which is very close to ideal shear strength of  $1.42\text{ GPa}$  for pure Au estimated by first-principle calculations.<sup>241</sup> In bulk materials with a high density of nanoscale twins, there is a twin spacing across which the deformation mechanism change from slip transferring across TBs for large twin spacing to easy dislocation nucleation from pre-existing sources for small twin spacing. Therefore, the maximum strength exists at this special twin spacing.<sup>215,242</sup> In contrast, the strength of NWs seems to increase with the decrease in the twin thickness until it is very close to or even reaches to the theoretical strength [Fig. 24(b)]. The corresponding deformation mechanism of the twinned NWs evolves from heterogeneous dislocation nucleation from free surface to homogeneous nucleation with reducing twin spacing in NWs.<sup>106</sup>

The strengthening effect of coherent twins in metallic NWs stems from the suppression of dislocation nucleation, which is not applicable to ceramic NWs due to the scarce of dislocation-mediated plasticity. However, a recent investigation proposed that GaAs NWs could be strengthened through planar defect engineering.<sup>58</sup> This strengthening effect was attributed to the higher Young's modulus values of the NWs with a high density of SFs, which makes the NWs more resistant to bending and better suppresses the crack initiation.<sup>71</sup> Most recently, *in-situ* tensile tests of SiC NWs with a highly defective 3C structure<sup>232</sup> demonstrated that there is a strong defect-density induced size effect on the fracture strength, increasing from  $8.1$  to  $25.3\text{ GPa}$  with the reduction of NW diameters from  $45$  to  $17\text{ nm}$ . These values are generally larger than those of SiC NWs with the perfect 3C crystalline structure. The highest fracture strength is very close to the ideal strength of 3C SiC. In fact, reducing the diameter of SiC NWs reduces the density of defects in the NWs and this increases the fracture strength of the NWs. Therefore, the size effect in this study was due to the size-dependent

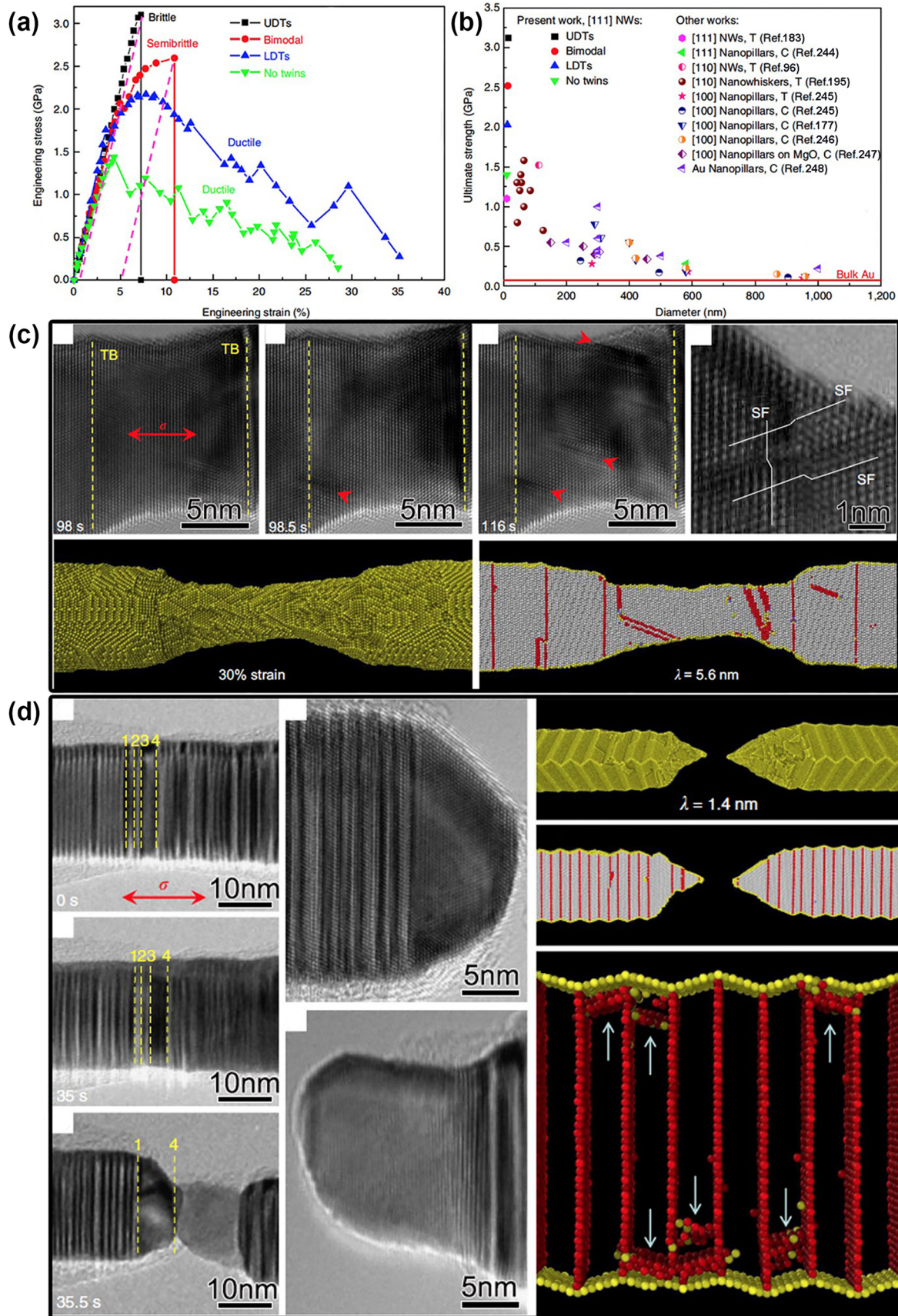


FIG. 24. (a) Typical stress-strain curves for Au Nws with no twins, a low-density of twins (LDTs), bimodal twin density of twins, and an ultrahigh density of twins (UDTs). (b) Comparison of ultimate strengthens in Au nanocrystals.<sup>244–248</sup> (c) The heterogeneous dislocation nucleation from surface in a Au NW with low-density twins revealed by the *in-situ* atomic scale deformation and MD simulation. (d) Brittle-like fracture in a Au NW with ultrahigh-density twins validated by experiments and MD simulation, while MD simulation confirmed that the brittle fracture originate from the homogeneous nucleation of dislocations.<sup>106</sup> Reprinted with permission from Wang *et al.*, Nat. Commun. **4**, 1742 (2013). Copyright 2013 Nature Publishing Group.

defect density rather than surface effect that is common to single crystalline NWs without planar defects.

In contrast to the dislocation starvation of single crystalline NWs during plastic deformation that leads to negligible strain hardening behaviour, internal planar defects will extensively interact with dislocations and provide ample room for dislocation storage to maintain the plastic flow. For example, Au NWs with a low density of twins yielded at  $\sim 1.7$  GPa and then the flow stress increases to the ultimate strength of  $\sim 2.05$  GPa due to the significant strain hardening, while no strain-hardening was observed for single crystalline Au NWs without planar defect. Molecular dynamics simulations revealed that ultrahigh plastic flow and strain hardening can be enabled in NWs with twinned structures when balancing NW diameter and TB spacing at the nanoscale.<sup>233</sup> Apart from the NWs with twins perpendicular to the NW axial direction, strain hardening was also observed in Ag NWs with fivefold twins parallel to longitudinal axis of the NWs, evidenced by the fact that the ultimate tensile strength is much higher than the yield strength for most of the tested samples.<sup>113,114</sup> Such hardening response can be attributed to the obstruction of surface-nucleated dislocations by TBs. In addition, the size-dependent strain hardening in this kind of NWs was also found.<sup>113,243</sup> Reducing the NW diameter reduces the effective distance between surface dislocation sources and TBs, which consequently increases the interactions between the TBs and surface dislocation sources. Therefore, the strain hardening and tensile ductility of NWs can be finely tuned by engineering the planar defects.

Twinned structures also have a significant effect on the deformation mechanisms of metallic NWs because the competition between various deformation mechanisms is influenced by twin thickness.<sup>106,121,235,242</sup> Reducing the twin thickness leads to the transformation from full dislocation activities to partial dislocation activities.<sup>121</sup> For Ni NWs with no twin or twin thickness ( $\lambda$ )  $> \sim 12$  nm, the plasticity is mediated by full dislocation activities. Both partial and full dislocation nucleation from the free surface was observed in NWs with twin thicknesses of  $\sim 9$  nm  $< \lambda < \sim 12$  nm. When twin thickness further reduced to below  $\sim 9$  nm, partial dislocations nucleated from the free surface dominate the plastic deformation.<sup>121</sup> In the case of nanocrystalline materials,<sup>199</sup> the preference for full or partial dislocations is determined by the critical resolved shear stresses needed for the nucleation of a perfect dislocation ( $\tau_N$ ) and a partial dislocation nucleation ( $\tau_p$ ), which is a function of grain size. When considering the twin thickness in NWs as the grain size of nanocrystalline materials,  $\tau_p$  becomes smaller than  $\tau_N$  when the twin thickness is smaller than a critical value ( $D_c$ ), determined by  $D_c = \frac{2\alpha\mu(b_N - b_p)b_p}{\gamma}$ <sup>199</sup> where  $\alpha$  equals to 0.5 and 1.5 for edge and screw dislocations, respectively,  $\mu$  is the shear modulus,  $\gamma$  is the SF energy, and  $b_N$  and  $b_p$  are the magnitudes of the Burgers vectors of the full and partial dislocations, respectively. There is a transition from full dislocation activities to partial dislocation activities as the twin thickness decreases to below  $D_c$ . The  $D_c$  for Ni NWs ranges from  $\sim 11$  to 22 nm. In addition to the heterogeneous dislocation nucleation from the free surface, the plasticity of NWs can be mediated by homogeneous

dislocation nucleation if the twin thickness decreased to a critical value. A series of *in-situ* tensile tests on Au NWs with orthogonally oriented twins showed a sharp transition from ductile fracture to brittle-like fracture with the decrease in the twin thickness, as revealed in Fig. 24(a).<sup>106</sup> The deformation of Au NWs with no twin or with a relatively low density of twins (twin thickness  $> 2.8$  nm) is dominated by partial dislocations heterogeneously nucleated from free surfaces, which gives rise to the sizeable ductility, as exhibited by experiments and MD simulations in Fig. 24(c). However, for Au NWs with an ultrahigh density of twins (twin thickness  $< 2.8$  nm), brittle-like fracture occurred due to the homogenous nucleation of dislocations, which was solely found near surface facets but inside the NW [Fig. 24(d)]. Homogenous dislocation nucleation is rapidly followed by plastic shear localisation when dislocations transmit through the TBs.<sup>233</sup> Although necking occurs, highly localised shear deformation accelerates the state of instability and result in the limited ductility and finally brittle-like fracture, as reflected by the stress-strain curve in Fig. 24(a).

It is interesting that twin thickness affects the gliding plane of dislocations, which can be either intersect with or parallel to the TBs. *In-situ* deformation HRTEM observations of Ni NWs with growth twins nearly parallel but in 7°-difference orientation with the NW axis<sup>121</sup> showed that for NWs with a twin thickness of  $\sim 6$  nm  $< \lambda \leq 9$  nm, partial dislocations intersecting with TBs were frequently observed. When reducing the twin thickness to  $\sim 1$  nm  $< \lambda \leq 6$  nm, partial dislocations glided on the plane parallel to the TBs. As the twin thickness decreased to  $\lambda \leq 1$  nm, partial dislocations glided on the plane parallel and adjacent to the TBs, resulting in TBs migration and de-twinning. Similar behaviours were also observed in the orthogonally twinned Au NWs with a twin thickness of  $\sim 0.7$  nm.<sup>106</sup> In a word, twin thickness in NWs plays an essential role in the dislocation behaviour including the nucleation choice of dislocation type (full or partial dislocations), nucleation mechanisms (heterogeneous or homogeneous), and the interaction modes with TBs.

Compared with most NWs with twins lying on the cross-section of the NWs, fivefold twinned or penta-twinned NWs, which contain five TBs running in parallel to the NW axis, are another type of twin-structured NWs. For perfect FCC triangular subunits, the angle between adjacent {111} facets is 70.53°. However, the angle that is required to create a fivefold twinned NW is 72°.<sup>234,249</sup> Elastic strains and stresses are, therefore, needed to accommodate 7.35° [(72° – 70.53°) × 5 = 7.35°] angular deficiency.<sup>216</sup> The NWs are expected to exhibit unusual plasticity due to their intrinsically strained structures.<sup>112,114,234,249–252</sup> Irrespective of the diameters of NWs, the metallic NWs with a penta-twinned structure always exhibit higher strain hardening ability than single crystalline NWs and other nanostructures.<sup>113,114,250</sup> *In-situ* tensile testing in SEM revealed that the strain hardening of fivefold twinned Ag NWs is size dependent, i.e., smaller NWs achieved more hardening, larger ultimate tensile strength, and higher tensile ductility than large ones.<sup>113</sup> MD simulations validated that strain hardening behaviour in these NWs can be attributed to the TB-mediated hardening mechanisms, i.e., nucleation-transmission events of partial

dislocations, leading to a chain of 3D stacking fault defects, while the size effect on strain hardening originated from the obstruction of dislocations by TBs since decreasing the diameter of NWs reduces the effective distance between TBs and the surface dislocation sources that leads to stronger dislocation–TB interactions.<sup>113</sup>

Another extraordinary mechanical behaviour found in the fivefold twinned Ag NWs is the time-dependent and fully reversible plasticity.<sup>112</sup> The stress–strain curve (Fig. 25) from the *in-situ* tensile test of a fivefold twinned Ag NW shows stress relaxation on loading while the actuator displacement was held constant, and complete plastic strain recovery on unloading. Experimental results indicated that stress relaxation and strain recovery were accompanied by the nucleation and annihilation of dislocations, respectively. MD simulations revealed that vacancy defects near the TB assist the nucleation of leading partial dislocations by reducing the dislocation nucleation barrier.<sup>112</sup> The observed complete recovery of plastic strain is attributed to the reverse motion of partial dislocations. TBs are effective obstacles to prevent the dislocation escaping from the free surface, and can also produce a repulsive force to drive the reverse motion of dislocations during unloading, which is also facilitated by the inhomogeneous stress field intrinsically generated by the five-fold twin. In addition, it was revealed that the relaxation time is size dependent, i.e., with the decrease in the diameter of NWs, the relaxation time increases, which is essentially attributed to the size effect of dislocation nucleation. All in all, engineering planar defects open up a window of opportunity to fabricate NWs with superior properties, which will be highly beneficial for the design and development of novel nanodevices with excellent functionality through manipulating the density and distribution of planar defects.

## V. SUMMARY AND CONCLUDING REMARKS

In the last 20 years, the success in high yield fabrication techniques of NWs offers great promise to various

applications of NWs in next generation electronic, electro-mechanical, and energy harvesting devices. Thorough understanding of the mechanical behaviours of NWs is critical prior to their successful integration into optimized reliable devices. This article summarizes the mechanical characterization techniques of NWs and reviews the mechanical properties of metallic and ceramic NWs. Almost all mechanical characterization techniques of NWs take advantage of various types of microscopes (TEM, SEM, or AFM) as a platform to visualize and manipulate small objects. Although nanomechanical testing of NWs remains challenging, mechanical characterization of NWs is a rapidly growing research field. The significant advancements in the experimental mechanics of NWs is benefiting from *in-situ* deformation techniques, which provide the possibility of direct dynamic observation of deformation mechanisms and simultaneous recording of stress–strain curves. Compared with *in-situ* SEM and AFM, *In-situ* TEM is more powerful, since TEM enables dimension measurement and local strain measurement at high accuracy, and offers the capability of defect identification at the atomic resolution.

The mechanical properties of NWs can be extracted from bending, uniaxial loading, resonance, and nanoindentation testing. Bending experiments are easy to perform because no complicated specimen preparation is needed and the testing can be completed in short time. However, the stress states of NWs under bending are complicated, which makes it difficult to build a direct relationship between deformation mechanisms and mechanical properties of NWs. Uniaxial tensile experiments provide relatively simple stress states of NWs, leading to easy interpretation of the measured mechanical data. However, it is difficult to conduct uniaxial loading experiments because of the difficulty of specimen preparation, which includes fixing and aligning NWs. In contrast, it is easy to carry out compression experiments but proper alignment of NWs to achieve uniaxial compression is difficult and this results in buckling of NWs and complicated stress status. While the resonance method is simple, it can only be used to extract the Young's modulus of NWs. Careful measurement of the NW shape and proper alignment between NW axial direction and loading direction can effectively reduce experimental errors.

Significant progress has been made in understanding the mechanical properties and deformation behaviors of metallic and semiconductor NWs. Although there is significant scattering in experimental results of Young's modulus, a majority of studies support the conclusion that the Young's modulus of NWs increases with the decrease in the diameter, and this can be explained based on the surface effect and the increase in surface-to-volume ratio with reducing NW diameter. Due to the largely increased critical resolved shear stress for plastic deformation under confined loading conditions in small volumes, ultrahigh elastic strain can be sustained in NWs.

Due to the extraordinary mechanical properties of NWs, including ultra-high elastic strains and yield strengths, NWs can be used in engineering structures of bulk materials to harvest outstanding mechanical performance. Recently, a nanostructured composite consisting of Nb NWs embedded in a NiTi matrix was successfully produced.<sup>27,28</sup> By

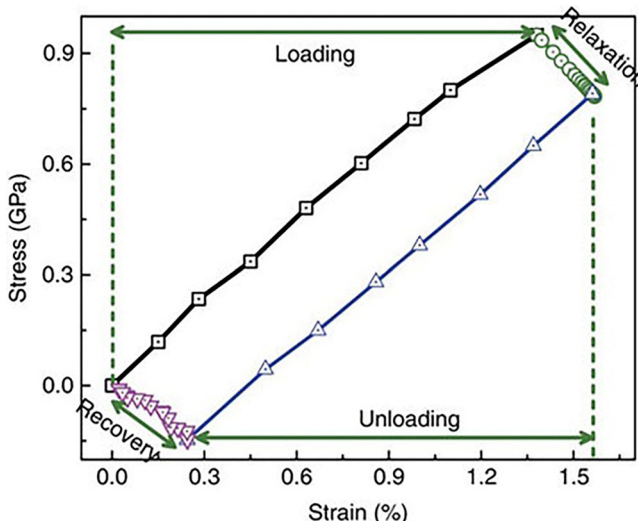


FIG. 25. Stress–strain curves for a penta-twinned Ag NW with a diameter of 120 nm.<sup>112</sup> Reprinted with permission from Qin *et al.*, Nat. Commun. **6**, 5983 (2015). Copyright 2015 Nature Publishing Group.

engineering the interfacial structure between the NWs and the matrix at the atomic scale and controlling residual stresses, combined high strength, high recoverable strain, and low stiffness were achieved in the composite. Taking advantage of the excellent properties of NWs in a bulk material setting provides new possibilities in materials design to accelerate the development of new materials with excellent mechanical properties.

Very high stress is required for new dislocation nucleation in a dislocation-starved state of NWs. This leads to ultrahigh strengths of NWs that are close to their theoretical strengths. Substantial size effects on the strength were observed, because of the diminished number of defects and the increased dislocation nucleation stress with reducing NW diameter. In terms of plastic properties, controversial results have been reported for the fracture mode of ceramic NWs because the mechanical behaviors of the NWs are complicated and depend on many factors, including strain rate, loading condition, NW size, NW orientation, and defects in the NWs. However, experimental results also demonstrated that reducing the diameter of NWs promotes plastic deformation. NWs are expected to be dislocation starved, therefore, plastic deformation of NWs are controlled by dislocation nucleation from the surface. A variety of deformation mechanisms including full dislocation slip, partial dislocation slip, and deformation twinning can occur in metal NWs. The choice of a particular deformation mode is influenced by many factors, including the crystallographic orientation and diameter of NWs, the orientation and roughness of NW side surfaces, the density of planar defects, and loading condition. Regarding to the large scatter and discrepancy in the reported mechanical properties of NWs, further systematic research is needed to reveal the reasons and to provide a comprehensive understanding of the underlying mechanisms.

Plastic deformation is non-recoverable or permanent in bulk materials. However, GaAs NWs under bending deformation and fivefold twinned Ag NWs under tension exhibit reversible plasticity, which is a result of the reverse motion and annihilation of dislocations during unloading driven by the large internal stress produced by the recovery of elastic strain in GaAs NWs, or the repulsive force produced by TBs in fivefold twinned Ag NWs.

Just as planar defects are critical in determining the mechanical behaviour of bulk metallic materials, crystalline defects also significantly affect the mechanical behaviours of NWs. Planar defects, including SFs and TBs, have stiffening and strengthening effects on NWs. Excellent strain hardening behaviour was observed in NWs with nano-twinned structures, because TBs act as barriers for dislocation motion, while no strain hardening was observed for single crystalline NWs without planar defect. Special twin structures in NWs also can render them unexpected time-dependent strain recovery capabilities, i.e., anelasticity. In addition to planar defects, grain boundaries also affect significantly the mechanical behaviors of polycrystalline materials. However, experimental studies on the structure–mechanical property relationships of polycrystalline NWs are still lacking. The effects of grain boundary structure and grain size on the atomistic deformation behaviors of

polycrystalline NWs can be explored using the *in-situ* deformation HRTEM technique.<sup>43,44</sup> It would be interesting to understand the combined effect of NW diameter and grain size on the deformation and to reveal which factor is more important in determining the deformation behaviors of polycrystalline NWs. Research in this area would extend the concept of grain boundary engineering to the research of the mechanical behavior of polycrystalline NWs and other low dimensional materials.

The ultra-high strength and superelasticity behaviours of NWs not only provide mechanical stability to their applications, but also the opportunity to tune their physico-chemical properties through elastic strain engineering, which endows new meaning to Feyman's statement “there's plenty of room at the bottom.” When the elastic strain of a material exceeds 1%, significant changes in carrier mobility, band gap, and thermoelectric properties, are expected to occur. Understanding the electrical properties of NWs corresponding to different strains is important for their applications, as well as elastic strain engineering. *In-situ* TEM holders that can be used to measure the electrical properties while straining have recently been commercially available, making it possible to expand the *in-situ* studies of nanomaterials from pure mechanical or electrical tests to electromechanical characterization.<sup>253</sup> To be specific, several fields can be explored in the near future, including the electromechanical responses of NWs (1) under different loading modes, (2) with different orientations, (3) with different crystalline structures, (4) with different NW diameters, and (5) with and without as-grown defects. Experiments that take advantage of state-of-the-art TEM facilities, including ultrafast TEM and aberration-corrected TEM, and *in-situ* techniques will provide insights into previously unobserved phenomena, including strain rate-dependent mechanical behaviors and strain-induced polarity in NWs. It is well known that doping via ion implantation is critical for the practical applications of the semiconductors. The ion implantation process usually introduces a large amount of crystalline defects into the semiconductor<sup>254,255</sup> and this is expected to have non-negligible influence on the mechanical properties of the materials. Investigation into the effect of irradiation defects on the mechanical behaviour of semiconductor NWs is therefore necessary. The aspect ratio of length to diameter has also been reported to affect significantly the mechanical behaviour of metallic pillars.<sup>256</sup> Although the deformation mechanisms of NWs might be different from that of metallic pillars, the aspect ratios of the NWs could affect the mechanical behaviour of the NWs. Further exploration of this issue is of fundamental significance as well.

## ACKNOWLEDGMENTS

X. Z. Liao was supported by the Australian Research Council under Grant Nos. FT110100236 and DP150101121. X. H. An was supported by the Australian Research Council under Grant No. DE170100053.

<sup>1</sup>C. M. Lieber, *MRS Bull.* **28**, 486 (2003).

<sup>2</sup>F. Qian, S. Gradecak, Y. Li, C. Y. Wen, and C. M. Lieber, *Nano Lett.* **5**, 2287 (2005).

- <sup>3</sup>P. D. Yang, *MRS Bull.* **30**, 85 (2005).
- <sup>4</sup>C. M. Lieber and Z. L. Wang, *MRS Bull.* **32**, 99 (2007).
- <sup>5</sup>D. E. Perea, N. Li, R. M. Dickerson, A. Misra, and S. T. Picraux, *Nano Lett.* **11**, 3117 (2011).
- <sup>6</sup>H. J. Joyce, J. Wong-Leung, Q. Gao, H. H. Tan, and C. Jagadish, *Nano Lett.* **10**, 908 (2010).
- <sup>7</sup>T. Burgess, S. Breuer, P. Caroff, J. Wong-Leung, Q. Gao, H. H. Tan, and C. Jagadish, *ACS Nano* **7**, 8105 (2013).
- <sup>8</sup>E. Kapon, D. M. Hwang, and R. Bhat, *Phys. Rev. Lett.* **63**, 430 (1989).
- <sup>9</sup>P. M. Petroff and G. Medeiros-Ribeiro, *MRS Bull.* **21**, 50 (1996).
- <sup>10</sup>Y. Cui, Q. Q. Wei, H. K. Park, and C. M. Lieber, *Science* **293**, 1289 (2001).
- <sup>11</sup>X. F. Duan, Y. Huang, Y. Cui, J. F. Wang, and C. M. Lieber, *Nature* **409**, 66 (2001).
- <sup>12</sup>J. F. Wang, M. S. Gudiksen, X. F. Duan, Y. Cui, and C. M. Lieber, *Science* **293**, 1455 (2001).
- <sup>13</sup>Y. Cui, Z. H. Zhong, D. L. Wang, W. U. Wang, and C. M. Lieber, *Nano Lett.* **3**, 149 (2003).
- <sup>14</sup>J. Hahn and C. M. Lieber, *Nano Lett.* **4**, 51 (2004).
- <sup>15</sup>Y. Huang and C. M. Lieber, *Pure Appl. Chem.* **76**, 2051 (2004).
- <sup>16</sup>Y. Huang, X. F. Duan, and C. M. Lieber, *Small* **1**, 142 (2005).
- <sup>17</sup>H. J. Joyce, Q. Gao, H. H. Tan, C. Jagadish, Y. Kim, J. Zou, L. M. Smith, H. E. Jackson, J. M. Yarrison-Rice, and P. Parkinson, *Prog. Quant. Electron.* **35**, 23 (2011).
- <sup>18</sup>C. Smith and M. E. Jones, *Superlattices Microstruct.* **4**, 391 (1988).
- <sup>19</sup>M. V. Fischetti and S. E. Laux, *J. Appl. Phys.* **80**, 2234 (1996).
- <sup>20</sup>M. V. Fischetti, F. Gämiz, and W. Hänsch, *J. Appl. Phys.* **92**, 7320 (2002).
- <sup>21</sup>J. Richter, O. Hansen, A. N. Larsen, J. L. Hansen, G. F. Eriksen, and E. V. Thomsen, *Sens. Actuators A* **123–124**, 388 (2005).
- <sup>22</sup>P. R. Chidambaram, C. Bowen, S. Chakravarthi, C. Machala, and R. Wise, *IEEE Trans. Electron Devices* **53**, 944 (2006).
- <sup>23</sup>M. E. Pistol and C. E. Pryor, *Phys. Rev. B* **80**, 035316 (2009).
- <sup>24</sup>J. Kim and M. V. Fischetti, *J. Appl. Phys.* **108**, 013710 (2010).
- <sup>25</sup>C. S. Smith, *Phys. Rev.* **94**, 42 (1954).
- <sup>26</sup>Y. Xiao, C. Meng, P. Wang, Y. Ye, H. K. Yu, S. S. Wang, F. X. Gu, L. Dai, and L. M. Tong, *Nano Lett.* **11**, 1122 (2011).
- <sup>27</sup>S. J. Hao, L. S. Cui, D. Q. Jiang, X. D. Han, Y. Ren, J. Jiang, Y. N. Liu, Z. Y. Liu, S. C. Mao, Y. D. Wang, Y. Li, X. B. Ren, X. D. Ding, S. Wang, C. Yu, X. B. Shi, M. S. Du, F. Yang, Y. J. Zheng, Z. Zhang, X. D. Li, D. E. Brown, and J. Li, *Science* **339**, 1191 (2013).
- <sup>28</sup>M. Zhou, *Science* **339**, 1161 (2013).
- <sup>29</sup>B. Wu, A. Heidelberg, and J. J. Boland, *Nat. Mater.* **4**, 525 (2005).
- <sup>30</sup>C. Herring and J. K. Galt, *Phys. Rev.* **85**, 1060 (1952).
- <sup>31</sup>S. S. Brenner, *J. Appl. Phys.* **27**, 1484 (1956).
- <sup>32</sup>R. E. Miller and V. B. Shenoy, *Nanotechnology* **11**, 139 (2000).
- <sup>33</sup>T. Zhu and J. Li, *Prog. Mater. Sci.* **55**, 710 (2010).
- <sup>34</sup>J. R. Greer and J. T. M. De Hosson, *Prog. Mater. Sci.* **56**, 654 (2011).
- <sup>35</sup>H. D. Espinosa, R. A. Bernal, and T. Filletre, *Small* **8**, 3233 (2012).
- <sup>36</sup>H. D. Espinosa, R. A. Bernal, and M. Minary-Jolandan, *Adv. Mater.* **24**, 4656 (2012).
- <sup>37</sup>L. H. Wang, Z. Zhang, and X. D. Han, *NPG Asia Mater.* **5**, e40 (2013).
- <sup>38</sup>H. S. Park, W. Cai, H. D. Espinosa, and H. C. Huang, *MRS Bull.* **34**, 178 (2009).
- <sup>39</sup>C. R. Weinberger and W. Cai, *J. Mater. Chem.* **22**, 3277 (2012).
- <sup>40</sup>S. Hoffmann, I. Utke, B. Moser, J. Michler, S. H. Christiansen, V. Schmidt, S. Senz, P. Werner, U. Gosele, and C. Ballif, *Nano Lett.* **6**, 622 (2006).
- <sup>41</sup>C. Y. Nam, P. Jaroenapibal, D. Tham, D. E. Luzzi, S. Evoy, and J. E. Fischer, *Nano Lett.* **6**, 153 (2006).
- <sup>42</sup>C. Q. Chen and J. Zhu, *Appl. Phys. Lett.* **90**, 043105 (2007).
- <sup>43</sup>X. D. Han, K. Zheng, Y. F. Zhang, X. N. Zhang, Z. Zhang, and Z. L. Wang, *Adv. Mater.* **19**, 2112 (2007).
- <sup>44</sup>X. D. Han, Y. F. Zhang, K. Zheng, X. N. Zhang, Z. Zhang, Y. J. Hao, X. Y. Guo, J. Yuan, and Z. L. Wang, *Nano Lett.* **7**, 452 (2007).
- <sup>45</sup>S. Hoffmann, F. Oestlund, J. Michler, H. J. Fan, M. Zacharias, S. H. Christiansen, and C. Ballif, *Nanotechnology* **18**, 205503 (2007).
- <sup>46</sup>Y. F. Zhang, X. D. Han, K. Zheng, Z. Zhang, X. N. Zhang, J. Y. Fu, Y. Ji, Y. J. Hao, X. Y. Guo, and Z. L. Wang, *Adv. Funct. Mater.* **17**, 3435 (2007).
- <sup>47</sup>B. M. Wen, J. E. Sader, and J. J. Boland, *Phys. Rev. Lett.* **101**, 175502 (2008).
- <sup>48</sup>M. J. Gordon, T. Baron, F. Dhalluin, P. Gentile, and P. Ferret, *Nano Lett.* **9**, 525 (2009).
- <sup>49</sup>K. Zheng, X. D. Han, L. H. Wang, Y. F. Zhang, Y. H. Yue, Y. Qin, X. N. Zhang, and Z. Zhang, *Nano Lett.* **9**, 2471 (2009).
- <sup>50</sup>Y. Zhu, F. Xu, Q. Q. Qin, W. Y. Fung, and W. Lu, *Nano Lett.* **9**, 3934 (2009).
- <sup>51</sup>F. Xu, Q. Q. Qin, A. Mishra, Y. Gu, and Y. Zhu, *Nano Res.* **3**, 271 (2010).
- <sup>52</sup>J. J. Brown, A. I. Baca, K. A. Bertness, D. A. Dikin, R. S. Ruoff, and V. M. Bright, *Sens. Actuator A* **166**, 177 (2011).
- <sup>53</sup>M. S. Steighner, L. P. Snedeker, B. L. Boyce, K. Gall, D. C. Miller, and C. L. Muhlstein, *J. Appl. Phys.* **109**, 033503 (2011).
- <sup>54</sup>Y. B. Wang, L. F. Wang, H. J. Joyce, Q. Gao, X. Z. Liao, Y.-W. Mai, H. H. Tan, J. Zou, S. P. Ringer, H. J. Gao, and C. Jagadish, *Adv. Mater.* **23**, 1356 (2011).
- <sup>55</sup>L. H. Wang, K. Zheng, Z. Zhang, and X. D. Han, *Nano Lett.* **11**, 2382 (2011).
- <sup>56</sup>Y. H. Yue, P. Liu, Z. Zhang, X. D. Han, and E. Ma, *Nano Lett.* **11**, 3151 (2011).
- <sup>57</sup>D.-M. Tang, C.-L. Ren, M.-S. Wang, X. L. Wei, N. Kawamoto, C. Liu, Y. Bando, M. Mitome, N. Fukata, and D. Golberg, *Nano Lett.* **12**, 1898 (2012).
- <sup>58</sup>B. Chen, J. Wang, Q. Gao, Y. J. Chen, X. Z. Liao, C. S. Lu, H. H. Tan, Y.-W. Mai, J. Zou, S. P. Ringer, H. J. Gao, and C. Jagadish, *Nano Lett.* **13**, 4369 (2013).
- <sup>59</sup>K. Kang and W. Cai, *Philos. Mag.* **87**, 2169 (2007).
- <sup>60</sup>Y. H. Wen, Z. Z. Zhu, and R. Z. Zhu, *Comput. Mater. Sci.* **41**, 553 (2008).
- <sup>61</sup>Y. H. Jing, Q. Y. Meng, and Y. F. Gao, *Comput. Mater. Sci.* **45**, 321 (2009).
- <sup>62</sup>K. Kang and W. Cai, *Int. J. Plast.* **26**, 1387 (2010).
- <sup>63</sup>W. W. Liang, M. Zhou, and F. J. Ke, *Nano Lett.* **5**, 2039 (2005).
- <sup>64</sup>J. Li, *MRS Bull.* **32**, 151 (2007).
- <sup>65</sup>B. Lee and R. E. Rudd, *Phys. Rev. B* **75**, 041305 (2007).
- <sup>66</sup>B. Lee and R. E. Rudd, *Phys. Rev. B* **75**, 195328 (2007).
- <sup>67</sup>L. H. Wang, P. Liu, P. F. Guan, M. J. Yang, J. L. Sun, Y. Q. Cheng, A. Hirata, Z. Zhang, E. Ma, M. W. Chen, and X. D. Han, *Nat. Commun.* **4**, 2413 (2013).
- <sup>68</sup>D. A. Dikin, X. Chen, W. Ding, G. Wagner, and R. S. Ruoff, *J. Appl. Phys.* **93**, 226 (2003).
- <sup>69</sup>C. Q. Chen, Y. Shi, Y. S. Zhang, J. Zhu, and Y. J. Yan, *Phys. Rev. Lett.* **96**, 075505 (2006).
- <sup>70</sup>K. H. Liu, W. L. Wang, Z. Xu, L. Liao, X. D. Bai, and E. G. Wang, *Appl. Phys. Lett.* **89**, 221908 (2006).
- <sup>71</sup>Y. J. Chen, T. Burgess, X. H. An, Y.-W. Mai, H. H. Tan, J. Zou, S. P. Ringer, C. Jagadish, and X. Z. Liao, *Nano Lett.* **16**(3), 1911–1916 (2016).
- <sup>72</sup>Y. J. Chen, Q. Gao, Y. B. Wang, X. H. An, X. Z. Liao, Y.-W. Mai, H. H. Tan, J. Zou, S. P. Ringer, and C. Jagadish, *Nano Lett.* **15**, 5279 (2015).
- <sup>73</sup>R. Agrawal, B. Peng, E. E. Gdoutos, and H. D. Espinosa, *Nano Lett.* **8**, 3668 (2008).
- <sup>74</sup>X. D. Li, H. S. Gao, C. J. Murphy, and K. K. Caswell, *Nano Lett.* **3**, 1495 (2003).
- <sup>75</sup>G. Feng, W. D. Nix, Y. Yoon, and C. J. Lee, *J. Appl. Phys.* **99**, 074304 (2006).
- <sup>76</sup>H. Ni and X. D. Li, *Nanotechnology* **17**, 3591 (2006).
- <sup>77</sup>J. H. Song, X. D. Wang, E. Riedo, and Z. L. Wang, *Nano Lett.* **5**, 1954 (2005).
- <sup>78</sup>E. W. Wong, P. E. Sheehan, and C. M. Lieber, *Science* **277**, 1971 (1997).
- <sup>79</sup>K. Davami, B. Mortazavi, H. M. Ghassemi, R. S. Yassar, J.-S. Lee, Y. Remond, and M. Meyyappan, *Nanoscale* **4**, 897 (2012).
- <sup>80</sup>A. San Paulo, J. Bokor, R. T. Howe, R. He, P. Yang, D. Gao, C. Carraro, and R. Maboudian, *Appl. Phys. Lett.* **87**, 053111 (2005).
- <sup>81</sup>G. Y. Jing, H. L. Duan, X. M. Sun, Z. S. Zhang, J. Xu, Y. D. Li, J. X. Wang, and D. P. Yu, *Phys. Rev. B* **73**, 235409 (2006).
- <sup>82</sup>H. Ni, X. D. Li, and H. S. Gao, *Appl. Phys. Lett.* **88**, 043108 (2006).
- <sup>83</sup>E. P. S. Tan, Y. Zhu, T. Yu, L. Dai, C. H. Sow, V. B. C. Tan, and C. T. Lim, *Appl. Phys. Lett.* **90**, 163112 (2007).
- <sup>84</sup>P.-H. Sung, C.-D. Wu, T.-H. Fang, and C.-I. Weng, *Appl. Surf. Sci.* **258**, 7064 (2012).
- <sup>85</sup>X. D. Han, Y. F. Zhang, X. Q. Liu, Z. Zhang, Y. J. Hao, and X. Y. Guo, *J. Appl. Phys.* **98**, 124307 (2005).
- <sup>86</sup>K. Zheng, C. C. Wang, Y.-Q. Cheng, Y. H. Yue, X. D. Han, Z. Zhang, Z. W. Shan, S. X. Mao, M. M. Ye, Y. D. Yin, and E. Ma, *Nat. Commun.* **1**, 24 (2010).
- <sup>87</sup>P. T. Bao, Y. B. Wang, X. Y. Cui, Q. Gao, H.-W. Yen, H. W. Liu, W. K. Yeoh, X. Z. Liao, S. C. Du, H. H. Tan, C. Jagadish, J. Zou, S. P. Ringer, and R. K. Zheng, *Appl. Phys. Lett.* **104**, 021904 (2014).

- <sup>88</sup>P. Jaroenapibal, D. E. Luzzi, S. Evoy, and S. Arepalli, *Appl. Phys. Lett.* **85**, 4328 (2004).
- <sup>89</sup>P. Poncharal, Z. L. Wang, D. Ugarte, and W. A. de Heer, *Science* **283**, 1513 (1999).
- <sup>90</sup>S. L. Wang, G. L. Chen, H. Huang, S. J. Ma, H. Y. Xu, Y. H. He, and J. Zou, *Nanotechnology* **24**, 505705 (2013).
- <sup>91</sup>H. F. Zhan and Y. Gu, *J. Appl. Phys.* **111**, 124303 (2012).
- <sup>92</sup>L. Meirovitch, *Elements of Vibration Analysis*, 2nd ed. (McGraw-Hill, New York, 1986).
- <sup>93</sup>S. Cuenot, C. Fretigny, S. Demoustier-Champagne, and B. Nysten, *Phys. Rev. B* **69**, 165410 (2004).
- <sup>94</sup>Z. Y. Gao, Y. Ding, S. S. Lin, Y. Hao, and Z. L. Wang, *Phys. Status Solidi RRL* **3**, 260 (2009).
- <sup>95</sup>P. F. Li, Q. L. Liao, S. Z. Yang, X. D. Bai, Y. H. Huang, X. Q. Yan, Z. Zhang, S. Liu, P. Lin, Z. Kang, and Y. Zhang, *Nano Lett.* **14**, 480 (2014).
- <sup>96</sup>J.-H. Seo, Y. Yoo, N.-Y. Park, S.-W. Yoon, H. Lee, S. Han, S.-W. Lee, T.-Y. Seong, S.-C. Lee, K.-B. Lee, P.-R. Cha, H. S. Park, B. Kim, and J.-P. Ahn, *Nano Lett.* **11**, 3499 (2011).
- <sup>97</sup>S. P. Timoshenko and J. M. Gere, *Theory of Elastic Stability*, 2nd ed. (McGraw-Hill, New York, 1961).
- <sup>98</sup>A. M. Minor, S. A. S. Asif, Z. W. Shan, E. A. Stach, E. Cyrankowski, T. J. Wyrobek, and O. L. Warren, *Nat. Mater.* **5**, 697 (2006).
- <sup>99</sup>Z. W. Shan, R. K. Mishra, S. A. S. Asif, O. L. Warren, and A. M. Minor, *Nat. Mater.* **7**, 115 (2008).
- <sup>100</sup>R. Nowak, D. Chrobak, S. Nagao, D. Vodnick, M. Berg, A. Tukiainen, and M. Pessa, *Nat. Nanotechnol.* **4**, 287 (2009).
- <sup>101</sup>J. Y. Huang, H. Zheng, S. X. Mao, Q. M. Li, and G. T. Wang, *Nano Lett.* **11**, 1618 (2011).
- <sup>102</sup>H. Guo, K. Chen, Y. Oh, K. Wang, C. Dejoie, S. A. S. Asif, O. L. Warren, Z. W. Shan, J. Wu, and A. M. Minor, *Nano Lett.* **11**, 3207 (2011).
- <sup>103</sup>D. Kiener and A. M. Minor, *Nano Lett.* **11**, 3816 (2011).
- <sup>104</sup>Y. Lu, J. Song, J. Y. Huang, and J. Lou, *Adv. Funct. Mater.* **21**, 3982 (2011).
- <sup>105</sup>B. Chen, Q. Gao, Y. B. Wang, X. Z. Liao, Y.-W. Mai, H. H. Tan, J. Zou, S. P. Ringer, and C. Jagadish, *Nano Lett.* **13**, 3169 (2013).
- <sup>106</sup>J. W. Wang, F. Sansoz, J. Y. Huang, Y. Liu, S. H. Sun, Z. Zhang, and S. X. Mao, *Nat. Commun.* **4**, 1742 (2013).
- <sup>107</sup>S. Dai, J. Zhao, M.-R. He, X. G. Wang, J. C. Wan, Z. W. Shan, and J. Zhu, *Nano Lett.* **15**, 8 (2015).
- <sup>108</sup>Y. J. Chen and X. Z. Liao, *Mechanical Behaviors of Semiconductor Nanowires in Semiconductors and Semimetals* (Academic Press, 2016), Chap. 4, Vol. 94, p. 109.
- <sup>109</sup>Y. B. Wang, C. C. Lee, J. Yi, X. H. An, M. X. Pan, K. Y. Xie, X. Z. Liao, J. M. Cairney, S. P. Ringer, and W. H. Wang, *Scr. Mater.* **84-85**, 27 (2014).
- <sup>110</sup>C. Chisholm, H. B. Bei, M. B. Lowry, J. Oh, S. A. S. Asif, O. L. Warren, Z. W. Shan, E. P. George, and A. M. Minor, *Acta Mater.* **60**, 2258 (2012).
- <sup>111</sup>Y. Zhu and H. D. Espinosa, *Proc. Natl. Acad. Sci. U.S.A.* **102**, 14503 (2005).
- <sup>112</sup>Q. Q. Qin, S. Yin, G. M. Cheng, X. Y. Li, T.-H. Chang, G. Richter, Y. Zhu, and H. J. Gao, *Nat. Commun.* **6**, 5983 (2015).
- <sup>113</sup>S. Narayanan, G. M. Cheng, Z. Zeng, Y. Zhu, and T. Zhu, *Nano Lett.* **15**, 4037 (2015).
- <sup>114</sup>Y. Zhu, Q. Q. Qin, F. Xu, F. R. Fan, Y. Ding, T. Zhang, B. J. Wiley, and Z. L. Wang, *Phys. Rev. B* **85**, 045443 (2012).
- <sup>115</sup>L. H. Wang, X. D. Han, P. Liu, Y. H. Yue, Z. Zhang, and E. Ma, *Phys. Rev. Lett.* **105**, 135501 (2010).
- <sup>116</sup>Y. H. Yue, P. Liu, Q. S. Deng, E. Ma, Z. Zhang, and X. D. Han, *Nano Lett.* **12**, 4045 (2012).
- <sup>117</sup>Y. H. Yue, N. K. Chen, X. B. Li, S. B. Zhang, Z. Zhang, M. W. Chen, and X. D. Han, *Nano Lett.* **13**, 3812 (2013).
- <sup>118</sup>L. H. Wang, J. Teng, P. Liu, A. Hirata, E. Ma, Z. Zhang, M. W. Chen, and X. D. Han, *Nat. Commun.* **5**, 4402 (2014).
- <sup>119</sup>Y. Lu, S. S. Xiang, L. R. Xiao, L. H. Wang, Q. S. Deng, Z. Zhang, and X. D. Han, *Sci. Rep.* **6**, 22937 (2016).
- <sup>120</sup>P. Liu, S. C. Mao, L. H. Wang, X. D. Han, and Z. Zhang, *Scr. Mater.* **64**, 343 (2011).
- <sup>121</sup>L. H. Wang, Y. Lu, D. L. Kong, L. R. Xiao, X. C. Sha, J. L. Sun, Z. Zhang, and X. D. Han, *Acta Mater.* **90**, 194 (2015).
- <sup>122</sup>D. L. Kong, S. D. Sun, T. J. Xin, L. R. Xiao, X. C. Sha, Y. Lu, S. C. Mao, J. Zou, L. H. Wang, and X. D. Han, *J. Alloys Compd.* **676**, 377 (2016).
- <sup>123</sup>S. X. Mao, M. H. Zhao, and Z. L. Wang, *Appl. Phys. Lett.* **83**, 993 (2003).
- <sup>124</sup>M. Lucas, W. J. Mai, R. S. Yang, Z. L. Wang, and E. Riedo, *Nano Lett.* **7**, 1314 (2007).
- <sup>125</sup>W. D. Callister and D. G. Rethwisch, *Materials Science and Engineering: An Introduction*, 8th ed. (John Wiley & Sons, Inc., New York, 2009).
- <sup>126</sup>L. G. Zhou and H. C. Huang, *Appl. Phys. Lett.* **84**, 1940 (2004).
- <sup>127</sup>H. Petrova, J. Perez-Juste, Z. Y. Zhang, J. Zhang, T. Kosel, and G. V. Hartland, *J. Mater. Chem.* **16**, 3957 (2006).
- <sup>128</sup>J. K. Diao, K. Gall, and M. L. Dunn, *J. Mech. Phys. Solids* **52**, 1935 (2004).
- <sup>129</sup>Z. M. Ao, S. Li, and Q. Jiang, *Appl. Phys. Lett.* **93**, 081905 (2008).
- <sup>130</sup>Y. J. Chen, X. H. An, X. Z. Liao, and Y.-W. Mai, *Nanotechnology* **26**, 435704 (2015).
- <sup>131</sup>M. T. McDowell, A. M. Leach, and K. Gall, *Nano Lett.* **8**, 3613 (2008).
- <sup>132</sup>G. Stan, C. V. Ciobanu, P. M. Parthangal, and R. F. Cook, *Nano Lett.* **7**, 3691 (2007).
- <sup>133</sup>A. Asthana, K. Momeni, A. Prasad, Y. K. Yap, and R. S. Yassar, *Nanotechnology* **22**, 265712 (2011).
- <sup>134</sup>A. J. Kulkarni, M. Zhou, and F. J. Ke, *Nanotechnology* **16**, 2749 (2005).
- <sup>135</sup>G. X. Cao and X. Chen, *Int. J. Solids Struct.* **45**, 3821 (2008).
- <sup>136</sup>H. Y. Liang, M. Upmanyu, and H. C. Huang, *Phys. Rev. B* **71**, 241403 (2005).
- <sup>137</sup>L. Y. Chen, G. Richter, J. P. Sullivan, and D. S. Gianola, *Phys. Rev. Lett.* **109**, 125503 (2012).
- <sup>138</sup>J. W. Christian and S. Mahajan, *Prog. Mater. Sci.* **39**, 1 (1995).
- <sup>139</sup>K. Otsuka and C. M. Wayman, *Shape memory materials*. (Cambridge university press, 1999).
- <sup>140</sup>K. A. Afanasyev and F. Sansoz, *Nano Lett.* **7**, 2056 (2007).
- <sup>141</sup>T. Y. Kim, S. S. Han, and H. M. Lee, *Mater. Trans.* **45**, 1442 (2004).
- <sup>142</sup>T. Kizuka, Y. Takatani, K. Asaka, and R. Yoshizaki, *Phys. Rev. B* **72**, 035333 (2005).
- <sup>143</sup>D. A. Smith, V. C. Holmberg, and B. A. Korgel, *ACS Nano* **4**, 2356 (2010).
- <sup>144</sup>P. G. Sanders, J. A. Eastman, and J. R. Weertman, *Acta Mater.* **45**, 4019 (1997).
- <sup>145</sup>A. J. Cao, Y. G. Wei, and E. Ma, *Phys. Rev. B* **77**, 195429 (2008).
- <sup>146</sup>J. J. Gilman, *Electronic Basis of the Strength of Materials* (Cambridge University Press, New York, 2003).
- <sup>147</sup>A. Rochefort, P. Avouris, F. Lesage, and D. R. Salahub, *Phys. Rev. B* **60**, 13824 (1999).
- <sup>148</sup>E. D. Minot, Y. Yaish, V. Sazonova, J. Y. Park, M. Brink, and P. L. McEuen, *Phys. Rev. Lett.* **90**, 156401 (2003).
- <sup>149</sup>K. H. Ahn, T. Lookman, and A. R. Bishop, *Nature* **428**, 401 (2004).
- <sup>150</sup>J. Cao, E. Ertekin, V. Srinivasan, W. Fan, S. Huang, H. Zheng, J. W. L. Yim, D. R. Khanal, D. F. Ogletree, J. C. Grossman, and J. Wu, *Nat. Nanotechnol.* **4**, 732 (2009).
- <sup>151</sup>T. Koga, X. Sun, S. B. Cronin, and M. S. Dresselhaus, *Appl. Phys. Lett.* **75**, 2438 (1999).
- <sup>152</sup>A. R. Abramson, C. L. Tien, and A. Majumdar, *Trans. ASME J. Heat Transfer* **124**, 963 (2002).
- <sup>153</sup>R. S. Jacobsen, K. N. Andersen, P. I. Borel, J. Fage-Pedersen, L. H. Frandsen, O. Hansen, M. Kristensen, A. V. Lavrinenko, G. Moulin, H. Ou, C. Peucheret, B. Zsigri, and A. Bjarklev, *Nature* **441**, 199 (2006).
- <sup>154</sup>V. M. Pereira and A. H. Castro Neto, *Phys. Rev. Lett.* **103**, 046801 (2009).
- <sup>155</sup>M. Jeong, B. Doris, J. Kedzierski, K. Rim, and M. Yang, *Science* **306**, 2057 (2004).
- <sup>156</sup>M. Chu, Y. K. Sun, U. Aghoram, and S. E. Thompson, *Annu. Rev. Mater. Res.* **39**, 203 (2009).
- <sup>157</sup>R. R. He and P. D. Yang, *Nat. Nanotechnol.* **1**, 42 (2006).
- <sup>158</sup>S. Cobo, J. Heidkamp, P.-A. Jacques, J. Fize, V. Fourmond, L. Guetaz, B. Jousselme, V. Ivanova, H. Dau, S. Palacin, M. Fontecave, and V. Artero, *Nat. Mater.* **10**, 807 (2011).
- <sup>159</sup>G. N. Greaves, A. L. Greer, R. S. Lakes, and T. Rouxel, *Nat. Mater.* **10**, 823 (2011).
- <sup>160</sup>G. Signorello, S. Karg, M. T. Björk, B. Gotsmann, and H. Riel, *Nano Lett.* **13**, 917 (2013).
- <sup>161</sup>E. K. McCarthy, A. T. Bellew, J. E. Sader, and J. J. Boland, *Nat. Commun.* **5**, 4336 (2014).
- <sup>162</sup>J. S. Juan, M. L. No, and C. A. Schuh, *Nat. Nanotechnol.* **4**, 415 (2009).
- <sup>163</sup>M. Wuttig and C. H. Lin, *Acta Metall.* **31**, 1117 (1983).
- <sup>164</sup>K. Miura, *Mater. Sci. Eng. A* **203**, 343 (1995).
- <sup>165</sup>L. S. Pan and S. Horibe, *Acta Mater.* **45**, 463 (1997).
- <sup>166</sup>H. Tanimoto, S. Sakai, and H. Mizubayashi, *Mater. Sci. Eng. A* **370**, 135 (2004).

- <sup>167</sup>A. Caron, A. Kawashima, H.-J. Fecht, D. V. Louguine-Luzquin, and A. Inoue, *Appl. Phys. Lett.* **99**, 171907 (2011).
- <sup>168</sup>A. Eichler, J. Moser, J. Chaste, M. Zdrojek, I. Wilson Rae, and A. Bachtold, *Nat. Nanotechnol.* **6**, 339 (2011).
- <sup>169</sup>M. K. Zalalutdinov, M. P. Ray, D. M. Photiadis, J. T. Robinson, J. W. Baldwin, J. E. Butler, T. I. Feygelson, B. B. Pate, and B. H. Houston, *Nano Lett.* **11**, 4304 (2011).
- <sup>170</sup>G. M. Cheng, C. Y. Miao, Q. Q. Qin, J. Li, F. Xu, H. Haftbaradaran, E. C. Dickey, H. J. Gao, and Y. Zhu, *Nat. Nanotechnol.* **10**, 687 (2015).
- <sup>171</sup>G. Schaumann, J. Völkl, and G. Alefeld, *Phys. Rev. Lett.* **21**, 891 (1968).
- <sup>172</sup>G. Schaumann, J. Völkl, and G. Alefeld, *Phys. Status Solidi B* **42**, 401 (1970).
- <sup>173</sup>J. Frenkel, *Z. Phys.* **37**, 572 (1926).
- <sup>174</sup>P. M. Anderson, J. P. Hirth, and J. Lothe, *Theory of Dislocations* (Cambridge University Press, Cambridge, 2017).
- <sup>175</sup>M. A. Meyers and K. K. Chawla, *Mechanical Behavior of Materials* (Cambridge University Press, Cambridge, 2009).
- <sup>176</sup>J. C. Fisher and J. H. Hollomon, *Trans. AIME* **171**, 546 (1947).
- <sup>177</sup>J. R. Greer and W. D. Nix, *Phys. Rev. B* **73**, 245410 (2006).
- <sup>178</sup>K. Gall, J. K. Diao, and M. L. Dunn, *Nano Lett.* **4**, 2431 (2004).
- <sup>179</sup>N. Agrait, G. Rubio, and S. Vieira, *Phys. Rev. Lett.* **74**, 3995 (1995).
- <sup>180</sup>H. D. Espinosa, B. C. Prorok, and B. Peng, *J. Mech. Phys. Solids* **52**, 667 (2004).
- <sup>181</sup>A. Kelly and N. H. Macmillan, *Strong Solids* (Oxford University Press, 1986).
- <sup>182</sup>C. Deng and F. Sansoz, *ACS Nano* **3**, 3001 (2009).
- <sup>183</sup>Y. Lu, J. Song, J. Y. Huang, and J. Lou, *Nano Res.* **4**, 1261 (2011).
- <sup>184</sup>G. Rubio-Bollinger, S. R. Bahn, N. Agrait, K. W. Jacobsen, and S. Vieira, *Phys. Rev. Lett.* **87**, 026101 (2001).
- <sup>185</sup>G. Richter, K. Hillerich, D. S. Gianola, R. Monig, O. Kraft, and C. A. Volkert, *Nano Lett.* **9**, 3048 (2009).
- <sup>186</sup>A. Paxton, P. Gumbsch, and M. Methfessel, *Philos. Mag. Lett.* **63**, 267 (1991).
- <sup>187</sup>J.-H. Seo, H. S. Park, Y. Yoo, T.-Y. Seong, J. Li, J.-P. Ahn, B. Kim, and I.-S. Choi, *Nano Lett.* **13**, 5112 (2013).
- <sup>188</sup>L. Y. Chen, M.-R. He, J. Shin, G. Richter, and D. S. Gianola, *Nat. Mater.* **14**, 707 (2015).
- <sup>189</sup>P. E. Marszalek, W. J. Greenleaf, H. Li, A. F. Oberhauser, and J. M. Fernandez, *Proc. Natl. Acad. Sci. U.S.A.* **97**, 6282 (2000).
- <sup>190</sup>J. K. Diao, K. Gall, and M. L. Dunn, *Nano Lett.* **4**, 1863 (2004).
- <sup>191</sup>J. K. Diao, K. Gall, M. L. Dunn, and J. A. Zimmerman, *Acta Mater.* **54**, 643 (2006).
- <sup>192</sup>X. Z. Liao, F. Zhou, E. J. Lavernia, S. G. Srinivasan, M. I. Baskes, D. W. He, and Y. T. Zhu, *Appl. Phys. Lett.* **83**, 632 (2003).
- <sup>193</sup>X. Z. Liao, Y. H. Zhao, S. G. Srinivasan, Y. T. Zhu, R. Z. Valiev, and D. V. Gunderov, *Appl. Phys. Lett.* **84**, 592 (2004).
- <sup>194</sup>S. Lee, J. Im, Y. Yoo, E. Bitzek, D. Kiener, G. Richter, B. Kim, and S. H. Oh, *Nat. Commun.* **5**, 3033 (2014).
- <sup>195</sup>A. Sedlmayr, E. Bitzek, D. S. Gianola, G. Richter, R. Mönig, and O. Kraft, *Acta Mater.* **60**, 3985 (2012).
- <sup>196</sup>J. W. Wang, Z. Zeng, C. R. Weinberger, Z. Zhang, T. Zhu, and S. X. Mao, *Nat. Mater.* **14**, 594 (2015).
- <sup>197</sup>Z. L. Wang, R. P. Gao, Z. W. Pan, and Z. R. Dai, *Adv. Eng. Mater.* **3**, 657 (2001).
- <sup>198</sup>Y. Lu and J. Lou, *Jom* **63**, 35 (2011).
- <sup>199</sup>M. W. Chen, E. Ma, K. J. Hemker, H. W. Sheng, Y. M. Wang, and X. M. Cheng, *Science* **300**, 1275 (2003).
- <sup>200</sup>S. H. Oh, M. Legros, D. Kiener, P. Gruber, and G. Dehm, *Acta Mater.* **55**, 5558 (2007).
- <sup>201</sup>H. Zheng, A. J. Cao, C. R. Weinberger, J. Y. Huang, K. Du, J. B. Wang, Y. Y. Ma, Y. N. Xia, and S. X. Mao, *Nat. Commun.* **1**, 144 (2010).
- <sup>202</sup>A. J. Cao, Y. G. Wei, and S. X. Mao, *Appl. Phys. Lett.* **90**, 151909 (2007).
- <sup>203</sup>H. S. Park, K. Gall, and J. A. Zimmerman, *J. Mech. Phys. Solids* **54**, 1862 (2006).
- <sup>204</sup>H. Van Swygenhoven, *Science* **296**, 66 (2002).
- <sup>205</sup>J. Y. Huang, Y. T. Zhu, X. Z. Liao, and R. Z. Valiev, *Philos. Mag. Lett.* **84**, 183 (2004).
- <sup>206</sup>L. Wang, D. Kong, T. Xin, X. Shu, K. Zheng, L. Xiao, X. Sha, Y. Lu, Z. Zhang, and X. Han, *Appl. Phys. Lett.* **108**, 151903 (2016).
- <sup>207</sup>Y.-J. Kim, K. Son, I.-C. Choi, I.-S. Choi, W. I. Park, and J.-i. Jang, *Adv. Funct. Mater.* **21**, 279 (2011).
- <sup>208</sup>D. F. Zhang, J.-M. Breguet, R. Clavel, V. Sivakov, S. Christiansen, and J. Michler, *J. Microelectromech. Syst.* **19**, 663 (2010).
- <sup>209</sup>J. Samuels, S. G. Roberts, and P. B. Hirsch, *Mater. Sci. Eng. A* **105–106**, 39 (1988).
- <sup>210</sup>M. Brede, *Acta Metall. Mater.* **41**, 211 (1993).
- <sup>211</sup>P. B. Hirsch and S. G. Roberts, *Acta Mater.* **44**, 2361 (1996).
- <sup>212</sup>Z. W. Pan, Z. R. Dai, and Z. L. Wang, *Appl. Phys. Lett.* **80**, 309 (2002).
- <sup>213</sup>Q. Zhang, J. J. Qi, Y. Yang, Y. H. Huang, X. Li, and Y. Zhang, *Appl. Phys. Lett.* **96**, 253112 (2010).
- <sup>214</sup>Y. H. Zhao, J. F. Bingert, X. Z. Liao, B. Z. Cui, K. Han, A. V. Sergueeva, A. K. Mukherjee, R. Z. Valiev, T. G. Langdon, and Y. T. Zhu, *Adv. Mater.* **18**, 2949 (2006).
- <sup>215</sup>L. Lu, X. Chen, X. X. Huang, and K. Lu, *Science* **323**, 607 (2009).
- <sup>216</sup>X. Y. Li, Y. J. Wei, L. Lu, K. Lu, and H. J. Gao, *Nature* **464**, 877 (2010).
- <sup>217</sup>S. Ni, Y. B. Wang, X. Z. Liao, R. B. Figueiredo, H. Q. Li, S. P. Ringer, T. G. Langdon, and Y. T. Zhu, *Acta Mater.* **60**, 3181 (2012).
- <sup>218</sup>X. H. Zhang, A. Misra, H. Wang, T. D. Shen, M. Nastasi, T. E. Mitchell, J. P. Hirth, R. G. Hoagland, and J. D. Embury, *Acta Mater.* **52**, 995 (2004).
- <sup>219</sup>X. H. Zhang, A. Misra, H. Wang, M. Nastasi, J. D. Embury, T. E. Mitchell, R. G. Hoagland, and J. P. Hirth, *Appl. Phys. Lett.* **84**, 1096 (2004).
- <sup>220</sup>X. H. Zhang, H. Wang, X. H. Chen, L. Lu, K. Lu, R. G. Hoagland, and A. Misra, *Appl. Phys. Lett.* **88**, 173116 (2006).
- <sup>221</sup>I. J. Beyerlein, X. H. Zhang, and A. Misra, *Annu. Rev. Mater. Res.* **44**, 329 (2014).
- <sup>222</sup>Y. T. Zhu, X. L. Wu, X. Z. Liao, J. Narayan, L. J. Kecskes, and S. N. Mathaudhu, *Acta Mater.* **59**, 812 (2011).
- <sup>223</sup>O. Anderoglu, A. Misra, H. Wang, and X. H. Zhang, *J. Appl. Phys.* **103**, 094322 (2008).
- <sup>224</sup>X. H. Zhang and A. Misra, *Scr. Mater.* **66**, 860 (2012).
- <sup>225</sup>L. Lu, Y. F. Shen, X. H. Chen, L. H. Qian, and K. Lu, *Science* **304**, 422 (2004).
- <sup>226</sup>O. Anderoglu, A. Misra, H. Wang, F. Ronning, M. F. Hundley, and X. H. Zhang, *Appl. Phys. Lett.* **93**, 083108 (2008).
- <sup>227</sup>B. D. Liu, Y. Bando, C. C. Tang, F. F. Xu, J. Q. Hu, and D. Golberg, *J. Phys. Chem. B* **109**, 17082 (2005).
- <sup>228</sup>Z. Chen, C. B. Cao, and H. S. Zhu, *Chem. Vap. Deposition* **13**, 527 (2007).
- <sup>229</sup>M. D. Kluge, D. Wolf, J. F. Lutsko, and S. R. Phillpot, *J. Appl. Phys.* **67**, 2370 (1990).
- <sup>230</sup>J. Schiotz, F. D. Di Tolla, and K. W. Jacobsen, *Nature* **391**, 561 (1998).
- <sup>231</sup>S.-F. Xie, S.-D. Chen, and A.-K. Soh, *Chin. Phys. Lett.* **28**, 066201 (2011).
- <sup>232</sup>G. M. Cheng, T.-H. Chang, Q. Q. Qin, H. C. Huang, and Y. Zhu, *Nano Lett.* **14**, 754 (2014).
- <sup>233</sup>C. Deng and F. Sansoz, *Nano Lett.* **9**, 1517 (2009).
- <sup>234</sup>J. H. Yoo, S. I. Oh, and M. S. Jeong, *J. Appl. Phys.* **107**, 094316 (2010).
- <sup>235</sup>C. Deng and F. Sansoz, *Appl. Phys. Lett.* **95**, 091914 (2009).
- <sup>236</sup>J. W. Wang, F. Sansoz, C. Deng, G. Xu, G. R. Han, and S. X. Mao, *Nano Lett.* **15**, 3865 (2015).
- <sup>237</sup>C. Deng and F. Sansoz, *Scr. Mater.* **63**, 50 (2010).
- <sup>238</sup>W. D. Luo, D. Roundy, M. L. Cohen, and J. W. Morris, Jr., *Phys. Rev. B* **66**, 094110 (2002).
- <sup>239</sup>D. M. Clatterbuck, C. R. Krenn, M. L. Cohen, and J. W. Morris, Jr., *Phys. Rev. Lett.* **91**, 135501 (2003).
- <sup>240</sup>H. P. Sheng, H. Zheng, F. Cao, S. J. Wu, L. Li, C. Liu, D. S. Zhao, and J. B. Wang, *Nano Res.* **8**, 3687 (2015).
- <sup>241</sup>S. Ogata, J. Li, N. Hirosaki, Y. Shibutani, and S. Yip, *Phys. Rev. B* **70**, 104104 (2004).
- <sup>242</sup>Y. T. Zhu, X. Z. Liao, and X. L. Wu, *Prog. Mater. Sci.* **57**, 1 (2012).
- <sup>243</sup>T. Filetter, S. Ryu, K. Kang, J. Yin, R. A. Bernal, K. Sohn, S. Li, J. Huang, W. Cai, and H. D. Espinosa, *Small* **8**, 2986 (2012).
- <sup>244</sup>A. S. Budiman, S. M. Han, J. R. Greer, N. Tamura, J. R. Patel, and W. D. Nix, *Acta Mater.* **56**, 602 (2008).
- <sup>245</sup>J.-Y. Kim and J. R. Greer, *Acta Mater.* **57**, 5245 (2009).
- <sup>246</sup>J. R. Greer, W. C. Oliver, and W. D. Nix, *Acta Mater.* **53**, 1821 (2005).
- <sup>247</sup>S.-W. Lee, S. M. Han, and W. D. Nix, *Acta Mater.* **57**, 4404 (2009).
- <sup>248</sup>C. A. Volkert and E. T. Lilleodden, *Philos. Mag.* **86**, 5567 (2006).
- <sup>249</sup>J. Y. Wu, S. Nagao, J. Y. He, and Z. L. Zhang, *Nano Lett.* **11**, 5264 (2011).
- <sup>250</sup>B. Wu, A. Heidelberg, J. J. Boland, J. E. Sader, X. M. Sun, and Y. D. Li, *Nano Lett.* **6**, 468 (2006).
- <sup>251</sup>A. J. Cao and Y. G. Wei, *Phys. Rev. B* **74**, 214108 (2006).
- <sup>252</sup>R. A. Bernal, A. Aghaei, S. Lee, S. Ryu, K. Sohn, J. Huang, W. Cai, and H. Espinosa, *Nano Lett.* **15**, 139 (2014).

- <sup>253</sup>Z. B. Chen, L. Hong, F. F. Wang, S. P. Ringer, L.-Q. Chen, H. S. Luo, and X. Z. Liao, *Phys. Rev. Lett.* **118**, 017601 (2017).
- <sup>254</sup>H. H. Tan, J. S. Williams, J. Zou, D. J. H. Cockayne, S. J. Pearson, and R. A. Stall, *Appl. Phys. Lett.* **69**, 2364 (1996).

- <sup>255</sup>S. O. Kucheyev, J. S. Williams, C. Jagadish, J. Zou, C. Evans, A. J. Nelson, and A. V. Hamza, *Phys. Rev. B* **67**, 094115 (2003).
- <sup>256</sup>D. Kiener, W. Grosse, G. Dehm, and R. Pippan, *Acta Mater.* **56**, 580 (2008).